Small signal analysis and dynamic modeling of a battery energy storage system in a DC microgrid

Rongrui Lin, Sungwoo Bae *

Power and Energy System Laboratory, Department of Electrical Engineering, Hanyang University, Seoul, 04763 South Korea

A R T I C L E   I N F O

A B S T R A C T

This paper presents a comprehensive small signal analysis of two types of battery energy storage systems (BESSs), including a voltage-controlled BESS (V-BESS) and a current-controlled BESS (C-BESS). This study also introduces dynamic models for integrating these two BESS configurations within a DC microgrid context. Through small signal analysis and participation factor analysis, this study investigates the interplay between the BESS and the DC microgrid and the internal interactions within the BESS. Subsequently, pivotal modeling parameters are discerned, and their impacts on system dynamics due to variations are unveiled through a sensitivity analysis. These results were verified through real-time software-in-the-loop simulations using an OPAL-RT 5707XH. Furthermore, this paper proposes dynamic models for both V-BESS and C-BESS integrated with a DC microgrid that can capture the dominant behavior of BESSs in a DC microgrid with relatively low computation demands. Potential applications of this study not only include providing a reference for modeling BESSs in a DC microgrid but also providing a guideline during the design and operation stages of a BESS in a DC microgrid. Finally, due to their modularity and scalability, the proposed dynamic models can be easily applied to the design and testing of BESS controllers.

1. Introduction

Due to the high penetration of renewable energy sources, battery energy storage systems (BESSs) are expected to play a pivotal role in future power systems. The production of renewable energy sources, such as photovoltaic and wind energy, has spatial–temporal uncertainty which can be addressed by incorporating an energy storage system in the power system [1]. The recent technological advancements and cost reduction in batteries have made the BESS a promising choice due to their obvious advances, such as high energy density, low self-discharge, and various application scenarios [2]. In the case of a power system, the capacity of the BESS can range from the megawatt level [3] to the household power level [4], and the applications of the BESS include complementing renewable energy sources [5], maintaining voltage stability [6], and providing frequency regulation [7]. However, the implementation of the BESS may also cause new challenges in the system dynamics, particularly stability issues due to its low inertia characteristics.

A proper BESS dynamic model is essential for studying the impact of BESS on power system dynamics [8], designing BESS controller parameters [9], and designing protection systems [10]. Moreover, an accurate and computationally efficient BESS model can facilitate new digital applications, such as digital twins and real-time simulations. Although nearly 25 % of publications in the field of energy digital twins are related to energy storage systems, the high computation cost of a complex model remains a critical issue [11]. Therefore, modeling BESSs applied to power systems is an enduring research topic [8,12–18]. Dynamic modeling of a BESS, which focuses on the stability study in large-scale power systems, was first proposed in [12]. This BESS dynamic model was applied to increase the damping of synchronous generator torsional oscillations. In contrast to the six-pulse converter examined in [8], [12] and [13] investigated a pulse-width modulated three-phase full-bridge voltage source converter in conjunction with a bi-directional buck-boost converter. Additionally, [8] discussed the stability impact of the battery bank configuration, BESS internal resistance, and BESS internal voltage in large-scale grids. The BESS modeling for the AC microgrid dynamic study, including comparative model studies with different levels of detail, can be found in [14]. In the article [19], the battery bank and its DC/DC converter were modeled as an ideal voltage source. There seems to be currently no consensus on the appropriate

---

* Corresponding author.
  E-mail address: swbae@hanyang.ac.kr (S. Bae).

Table 1
Summary of comparison in previous works.

Ref.	Inclusion of small signal analysis	Inclusion of sensitivity analysis	Research object	Target system	Limitation of the study
[8]	Yes	Yes	BESS	BESS connected to the point of common coupling.	Did not consider the connected system such as a microgrid
[12]	Yes	No	BESS	Power system with a generator and an infinite bus	Modelled the battery bank as a 1st-order Thevenin model
[13]	No	No	ESS	WSCC 9-bus test system	Modelled the battery bank as the Shepherd model
[14]	Yes	No	BESS	Modified version CIGRE benchmark AC microgrid	Did not provide a comprehensive small signal analysis
[15]	No	No	Battery cell	Battery pack	Employed a 1st-order Thevenin model to describe transient behaviors
[16]	No	No	BESS	Connect to the WSCC 9-bus system through a transformer	Only studied the impact of battery internal resistance and battery voltage
[17]	No	No	BESS	A 120 kV/60 Hz transmission system	Studied the behaviors of BESS under faults
[19]	No	No	Synchronous Generator	A 480Y/277 V AC microgrid	Modelled the battery bank and DC/DC converter as a simple voltage source
[25]	Yes	Yes	DC microgrid	A bipolar DC microgrid with PV and ESS	Studied the stability interactions among three bus ports
[26]	Yes	Yes	Parallel converters	A DC microgrid with a resistive load and a constant power load	Studied the interaction between converters
[27]	Yes	Yes	Supercapacitor and PV	A multi-bus DC microgrid which is operating in an islanding mode	Investigated the effects of the system parameters on the stability

model to be used for a BESS. Other applications of grid-level BESS dynamic models have also been investigated, such as inhomogeneous degradation [15], transmission systems [16], and grid fault analysis [17]. However, with new developments in power systems, emerging application environments have raised new requirements for the BESS dynamic modeling [20,21].

Few studies have covered a suitable BESS dynamic model for the DC microgrid dynamic study despite the increasing attention and wide applications of DC microgrids due to their advantages, such as high efficiency, larger capacity, and simple structure [22]. However, a DC microgrid has also faced stability challenges, such as low damping and negative impedance [23,24]. Some researchers [25–27] have endeavored to explore the stability of DC microgrid. In [25], the study investigated the interactions among different bus ports in a bipolar DC microgrid. DC microgrids may also have multiple parallel converters, among which interactions were investigated by the researchers in [26]. However, the authors in [26] overlooked the impact of sources connected to the converters. The stability impact of a hybrid source, consisting of a supercapacitor and a PV system on a DC microgrid, was explored in [27]. However, for studying the system dynamics of a BESS in a DC microgrid, the interaction mechanism between the BESS and the DC microgrid, as well as within the BESS, has not been clearly investigated as summarized in Table 1. When studying the dynamic behavior and impact of a BESS placed in a power system, in addition to the BESS itself, the rest of the system connected to it is also required to be considered [28]. Otherwise, it may lead researchers to build redundant, overly complex, or overly simplified models. At the battery cell level, researchers have primarily focused on modeling the interaction within battery cells [29]. Conversely, researchers have commonly utilized a constant voltage source at the power system level to represent the battery bank [8]. However, a crucial bridge between these two research areas currently seems to lack in selecting an appropriate battery bank model for the dynamic study of DC microgrids.

These problems make it challenging to select an appropriate BESS model for the DC microgrid dynamic study. A detailed model that captures all the essential information of BESS can provide accurate results, while it may be computationally expensive and unsuitable for promoting residential and small-scale applications [15]. In contrast, an overly simplified model may fail to capture critical information, leading to poor performance of the controller and protection system [17]. To suitably model the dynamic behavior of a BESS in a DC microgrid, it is crucial to identify which components are critical for the dynamic study and to understand the effect of their parameter variations. This model has

significant implications for the dynamic modeling of BESS in both the design and operation stages, as it allows for consideration of the necessary components during the design stage and the parameter variations affected due to the aging during the operation stage.

To address these challenges, this paper aims to study the interaction mechanism of a BESS in a DC microgrid and propose suitable BESS models that can capture the dominant behavior with relatively low computation demands. The main contributions of this study are:

- This paper presents a small signal analysis and a sensitivity analysis for two types of BESSs in a DC microgrid, with the inherent capacity to regulate their bus voltage, output reference current, or power. The interaction mechanism between the BESS and the DC microgrid, as well as within the BESS, is delved.
- This study identifies critical components necessary for the dynamic study of a BESS in a DC microgrid and assesses the effect of parameter variations. The conducted analysis not only serves as a reference for researchers considering necessary components in their models but also helps designers in adjusting parameters during the design stage to improve system dynamic performance.
- This study proposes new dynamic models for both types of BESS for the DC microgrid dynamic study, which can capture the dominant behavior of BESSs while requiring relatively low computation demands. The proposed models can be easily applied to the design and testing of BESS controllers due to their modularity and scalability.
- This study bridges the gap between battery cell and power system level research by selecting an appropriate battery bank model for the dynamic analysis of DC microgrids. This paper finds that the battery bank model only needs to consider the internal resistance and open-circuit voltage, which can reduce computational complexity without significantly affecting the accuracy of the results.

The paper is structured as follows: Section 2 describes fully detailed BESS models for both types, including every individual component. Section 3 reveals critical components for the dynamic study and the impact of their parameter variations through small signal analysis and sensitivity analysis, which will be further verified through real-time software-in-the-loop simulations in Section 4. Section 4 presents the proposed models compared with the detailed electromagnetic models explained in Section 2. Finally, Section 5 summarizes the paper with the main contributions and implications of the research.

Table 2
The performance of various ECMs.

| ECMs	A123 18,650 cell (LiFePO$_4$)		Samsung INR 18650-20R cell (Li-NiMnCoO$_2$)	
	MSE of US06	MSE of FUDS	MSE of US06	MSE of FUDS
Internal resistance model	104.99×10^{-5}	110.80×10^{-5}	33.61×10^{-5}	49.67×10^{-5}
1st-order Thevenin model	9.15×10^{-5}	17.14×10^{-5}	17.32×10^{-5}	17.57×10^{-5}
2nd-order Thevenin model	7.94×10^{-5}	8.87×10^{-5}	6.62×10^{-5}	5.40×10^{-5}
PNGV model	24.80×10^{-5}	47.32×10^{-5}	6.74×10^{-5}	10.42×10^{-5}
Modified saft-RC model	10.43×10^{-5}	18.43×10^{-5}	11.14×10^{-5}	19.10×10^{-5}
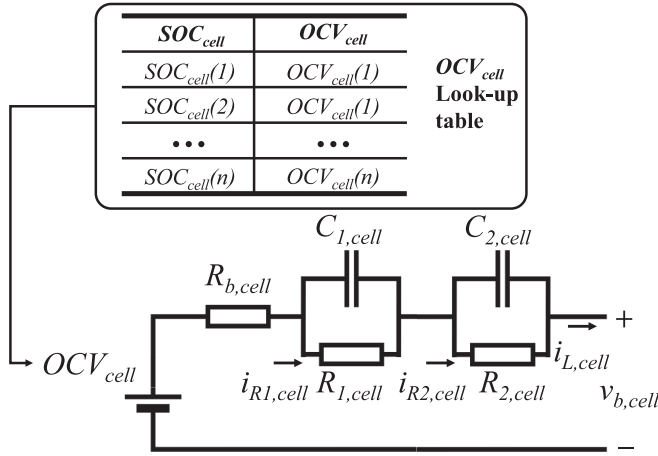
Fig. 1. 2nd–order Thevenin model of a battery cell [30].

2. System modeling

2.1. Overview

This section presents a comprehensive modeling approach for BESSs integrated into a DC microgrid. It includes accurate models for a battery bank, a bidirectional converter, controllers, and a generic DC microgrid. The proposed model also includes a bidirectional buck-boost converter (BBBC) and its controllers, commonly used in BESS applications. The proposed modeling approach ensures that all components are fully described, providing a comprehensive and accurate representation of a BESS in a DC microgrid. The modeling approach presented in this section serves as the foundation for the analysis and evaluation of the system in the following sections. This section also presents the comparison of different modeling methods to ensure the accuracy and suitability of the battery bank model.

2.2. Battery bank modeling

In this subsection, several equivalent circuit models (ECMs) of the battery cell are compared to find the battery model with the best performance. ECMs are widely applied in electrical research due to their ability to describe the current–voltage characteristics of the battery cell. The internal resistance model, different orders of the Thevenin models [30], the partnership for a new generation vehicles capacitance (PNGV) model [31], and the saft capacitance model [31] are representative and popular among the ECMs. Based on the model comparisons, one can determine the most accurate model to ensure the precision of our battery bank model.

Parameters of all models in this study were determined using the least squares method and datasets from CALCE Battery Research Group [32,33]. To standardize the identification process and improve the accuracy, the capacitor, which represents the energy storage in the battery cell and provides the open-circuit-voltage (OCV_{cell}), was replaced by a controllable ideal DC voltage source of which voltage is determined by a $SoC(State-of-Charge)-OCV_{cell}$ look-up table. Two types of battery cells were studied, including A123 18,650 cell (i.e., LiFePO4 battery) and Samsung INR 18650-20R cell (i.e., a Li-NiMnCoO2 battery). The parameters were identified using the dynamical stress testing (DST) dataset and tested using the US06 driving schedule and the federal driving urban driving schedule (FUDS) datasets provided by the CALCE Battery Research Group [32,33]. The mean square error (MSE) results of different ECMs are listed in Table 2. Based on the testing results, it can be concluded that the 2nd-order Thevenin model is the most accurate in describing the electrical characteristics of both types of battery cells.

The 2nd-order Thevenin model comprises a controllable ideal DC voltage source of which voltage is determined by the $SoC-OCV_{cell}$ look-up table in series with an internal resistance $R_{b,cell}$ and two resistance–capacitance pairs (RC pairs), as illustrated in Fig. 1. The parameters of the Thevenin model are the functions of temperature, SoC, State of Health (SoH). However, in the transient studies analyzed at the time scale order of seconds, the variations of these parameters over short durations can be disregarded [34–36]. Due to a self-discharge rate typically not exceeding 5 % per month in a battery cell, its impact can also be considered inconsequential, posing no risk of unacceptable errors [30]. Therefore, the dynamic behavior of a battery cell can be described as follows:

$$\begin{cases} \dfrac{di_{R1,cell}}{dt} = -\dfrac{1}{R_{1,cell}C_{1,cell}}i_{R1,cell} + \dfrac{1}{R_{1,cell}C_{1,cell}}i_{L,cell} \\ \dfrac{di_{R2,cell}}{dt} = -\dfrac{1}{R_{2,cell}C_{2,cell}}i_{R2,cell} + \dfrac{1}{R_{2,cell}C_{2,cell}}i_{L,cell} \\ v_{b,cell} = OCV_{cell} - i_{L,cell}R_{b,cell} - i_{R1,cell}R_{1,cell} - i_{R2,cell}R_{2,cell} \end{cases} \quad (1)$$

where $i_{R1,cell}$ and $i_{R2,cell}$ are the current flow through the resistance $R_{1,cell}$ and the resistance $R_{2,cell}$ respectively, $v_{b,cell}$ is the terminal voltage of the battery cell, $i_{L,cell}$ is the current flow through the resistance $R_{b,cell}$. From (1), it can be recognized that the current $i_{L,cell}$ equals the current $i_{R1,cell}$ and the current $i_{R2,cell}$ when the battery cell is working at a steady state. Furthermore, when the battery cell is experiencing a transient process, the time back to the steady state depends on the time constant $\tau_1 = R_{1,cell}C_{1,cell}$ and $\tau_2 = R_{2,cell}C_{2,cell}$. By using a big cell model [8], if the battery bank includes m cells connected in series and n cells connected in parallel, the battery bank can be modeled by

$$\begin{cases} \dfrac{di_{R1}}{dt} = -\dfrac{1}{R_1 C_1}i_{R1} + \dfrac{1}{R_1 C_1}i_L \\ \dfrac{di_{R2}}{dt} = -\dfrac{1}{R_2 C_2}i_{R2} + \dfrac{1}{R_2 C_2}i_L \\ v_b = OCV - i_L R_b - i_{R1}R_1 - i_{R2}R_2 \end{cases} \quad (2)$$

where the $OCV = m \times OCV_{cell}$, $R_1 = m/n \times R_{1,cell}$, $R_2 = m/n \times R_{2,cell}$, $C_1 = n/m \times C_{1,cell}$, $C_2 = n/m \times C_{2,cell}$, and $R_b = m/n \times R_{b,cell}$. From (2), it can be seen that the dynamic time constants τ_1 and τ_2 of the battery bank are the same as those of a single battery cell.

2.3. Converter and its controller modeling

The BBBC and its controllers are responsible for connecting the battery bank to the DC microgrid. The schematic diagram of the BBBC and its controllers studied in this paper is depicted in Fig. 2. BESS applications can be divided into two types in a DC microgrid. The first type uses a controller that aims to support the voltage stability of the DC bus and ensure power balance [37]. The second type employs a controller that makes the BESS a constant current source/load or constant power
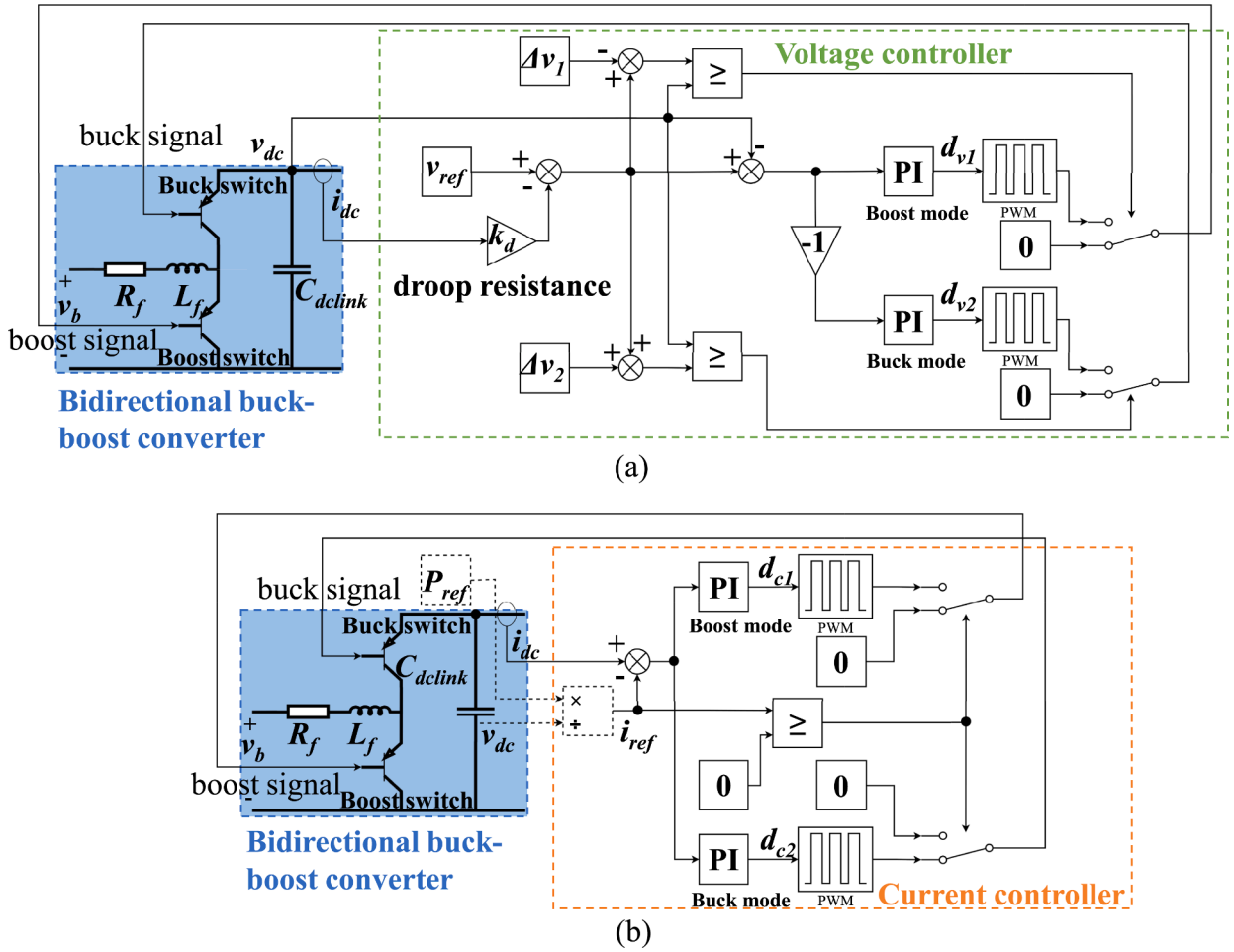
Fig. 2. (a) Voltage controller for a bidirectional buck-boost converter; (b) Current controller for a bidirectional buck-boost converter.

source/load [38]. To study the dynamics of BESS, this paper proposes two generic controllers that can be respectively used in these two types of BESS. As illustrated in Fig. 2, the voltage controller uses a reference voltage, while the current controller uses a reference current or reference power. The reference values for both controllers can be generated by upper-level controllers. The voltage-controlled BESS (V-BESS) has a voltage controller to ensure voltage stability and power balance. The current-controlled BESS (C-BESS) has a current controller and provides a constant current or power source/load.

Depending on the operational requirements of the DC microgrid, the BBBC can operate in either the buck mode or the boost mode. When the DC microgrid requires the BESS to export power, the BBBC runs in the boost mode. In this mode, the buck switch is always turned off, while the boost switch is controlled by the modulation signal from the PWM. The battery bank is discharged during the boost mode. Conversely, if the DC microgrid needs the BESS to absorb excess power, the BBBC will operate in the buck mode. Here, the boost switch is always in the open state, while the buck switch is controlled by the modulation signal, and the battery bank is in the charging mode. If the duty cycle d is determinate, the battery discharging current i_L and the voltage v_{dc} at C_{dclink} can be described by the following equation:

$$\begin{cases} \dfrac{di_L}{dt} = \dfrac{1}{L_f}(v_b - i_L R_f - d v_{dc}) \\ \dfrac{dv_{dc}}{dt} = \dfrac{1}{C_{dclink}}(d i_L - i_{dc}) \end{cases} \quad (3)$$

where L_f is the inductance of the filter that should be chosen by considering the current ripple [14], R_f is the parasitic resistance of the
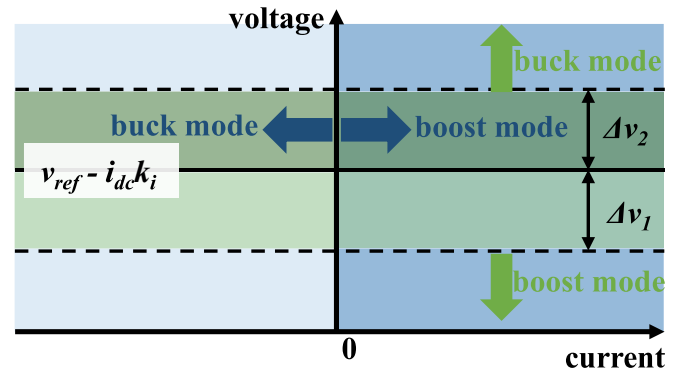

Fig. 3. Operational modes of the BESS with the proposed controllers.

filter, and i_{dc} is the current flowing out from the converter. The calculation method of the duty cycle received from the BBBC controller depends on the operation mode of the BESS. In the boost mode, a duty cycle equals $(1-d_{v1})$ or $(1-d_{c1})$, while a duty cycle is equal to d_{v2} or d_{c2} in the buck mode. When the voltage controller works in the boost mode, the duty cycle d_{v1} can be calculated as follows:

$$\begin{cases} \dfrac{dx_{v1}}{dt} = v_{ref} - i_{dc}k_d - v_{dc} \\ d_{v1} = k_{p,v1}(v_{ref} - i_{dc}k_d - v_{dc}) + k_{i,v1}x_{v1} \end{cases} \quad (4)$$

where x_{v1} is the state variable of the boost PI controller, $k_{p,v1}$ and $k_{i,v1}$
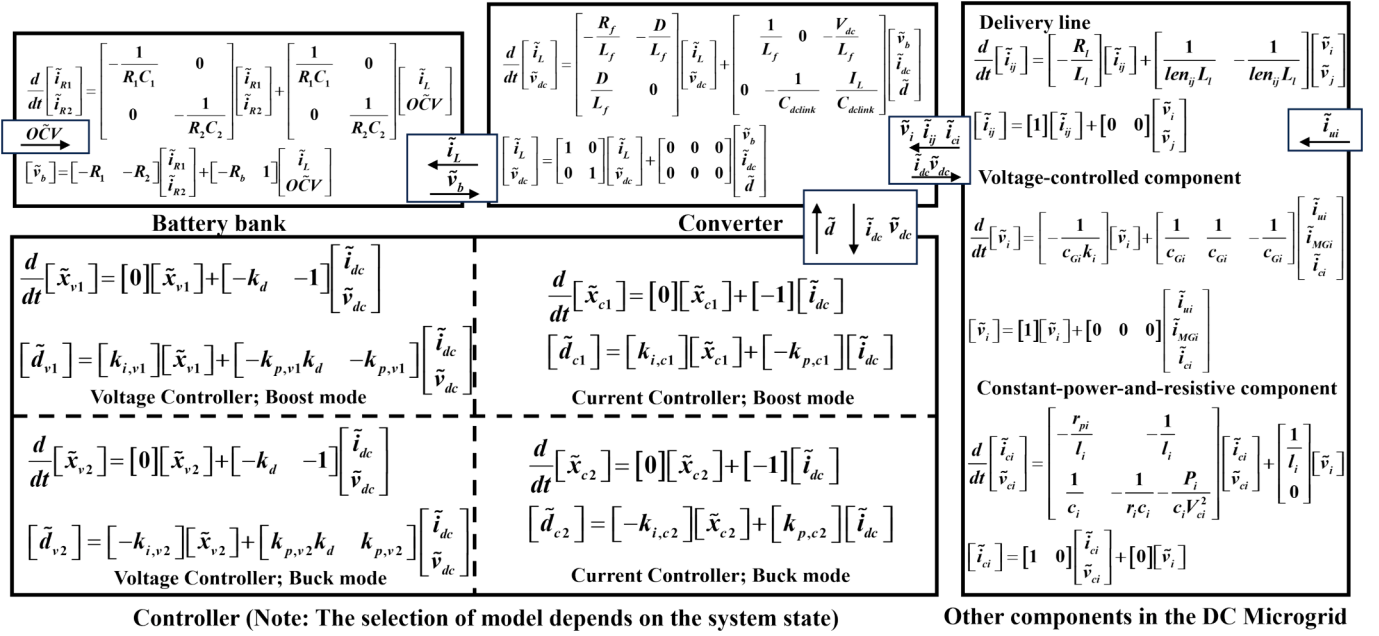
Battery bank

$$\frac{d}{dt}\begin{bmatrix}\tilde{i}_{R1}\\\tilde{i}_{R2}\end{bmatrix}=\begin{bmatrix}-\dfrac{1}{R_1C_1}&0\\[4pt]0&-\dfrac{1}{R_2C_2}\end{bmatrix}\begin{bmatrix}\tilde{i}_{R1}\\\tilde{i}_{R2}\end{bmatrix}+\begin{bmatrix}\dfrac{1}{R_1C_1}&0\\[4pt]0&\dfrac{1}{R_2C_2}\end{bmatrix}\begin{bmatrix}\tilde{i}_L\\O\check{C}V\end{bmatrix}$$

$$[\tilde{v}_b]=[-R_1\ \ -R_2]\begin{bmatrix}\tilde{i}_{R1}\\\tilde{i}_{R2}\end{bmatrix}+[-R_b\ \ 1]\begin{bmatrix}\tilde{i}_L\\O\check{C}V\end{bmatrix}$$

Converter

$$\frac{d}{dt}\begin{bmatrix}\tilde{i}_L\\\tilde{v}_{dc}\end{bmatrix}=\begin{bmatrix}-\dfrac{R_f}{L_f}&-\dfrac{D}{L_f}\\[4pt]\dfrac{D}{L_f}&0\end{bmatrix}\begin{bmatrix}\tilde{i}_L\\\tilde{v}_{dc}\end{bmatrix}+\begin{bmatrix}\dfrac{1}{L_f}&0&-\dfrac{V_{dc}}{L_f}\\[4pt]0&-\dfrac{1}{C_{dclink}}&\dfrac{I_L}{C_{dclink}}\end{bmatrix}\begin{bmatrix}\tilde{v}_b\\\tilde{i}_{dc}\\\tilde{d}\end{bmatrix}$$

$$\begin{bmatrix}\tilde{i}_L\\\tilde{v}_{dc}\end{bmatrix}=\begin{bmatrix}1&0\\0&1\end{bmatrix}\begin{bmatrix}\tilde{i}_L\\\tilde{v}_{dc}\end{bmatrix}+\begin{bmatrix}0&0&0\\0&0&0\end{bmatrix}\begin{bmatrix}\tilde{v}_b\\\tilde{i}_{dc}\\\tilde{d}\end{bmatrix}$$

Delivery line

$$\frac{d}{dt}[\tilde{i}_{ij}]=\left[-\frac{R_l}{L_l}\right][\tilde{i}_{ij}]+\left[\frac{1}{len_{ij}L_l}\ \ -\frac{1}{len_{ij}L_l}\right]\begin{bmatrix}\tilde{v}_i\\\tilde{v}_j\end{bmatrix}$$

$$[\tilde{i}_{ij}]=[1][\tilde{i}_{ij}]+[0\ \ 0]\begin{bmatrix}\tilde{v}_i\\\tilde{v}_j\end{bmatrix}$$

Voltage-controlled component

$$\frac{d}{dt}[\tilde{v}_i]=\left[-\frac{1}{c_{Gi}k_i}\right][\tilde{v}_i]+\left[\frac{1}{c_{Gi}}\ \ \frac{1}{c_{Gi}}\ \ -\frac{1}{c_{Gi}}\right]\begin{bmatrix}\tilde{i}_{ui}\\\tilde{i}_{MGi}\\\tilde{i}_{ci}\end{bmatrix}$$

$$[\tilde{v}_i]=[1][\tilde{v}_i]+[0\ \ 0\ \ 0]\begin{bmatrix}\tilde{i}_{ui}\\\tilde{i}_{MGi}\\\tilde{i}_{ci}\end{bmatrix}$$

Constant-power-and-resistive component

$$\frac{d}{dt}\begin{bmatrix}\tilde{i}_{ci}\\\tilde{v}_{ci}\end{bmatrix}=\begin{bmatrix}-\dfrac{r_{pi}}{l_i}&-\dfrac{1}{l_i}\\[6pt]\dfrac{1}{c_i}&-\dfrac{1}{r_ic_i}-\dfrac{P_i}{c_iV_i^2}\end{bmatrix}\begin{bmatrix}\tilde{i}_{ci}\\\tilde{v}_{ci}\end{bmatrix}+\begin{bmatrix}\dfrac{1}{l_i}\\[4pt]0\end{bmatrix}[\tilde{v}_i]$$

$$[\tilde{i}_{ci}]=[1\ \ 0]\begin{bmatrix}\tilde{i}_{ci}\\\tilde{v}_{ci}\end{bmatrix}+[0][\tilde{v}_i]$$

Controller (Note: The selection of model depends on the system state)

$$\frac{d}{dt}[\tilde{x}_{v1}]=[0][\tilde{x}_{v1}]+[-k_d\ \ -1]\begin{bmatrix}\tilde{i}_{dc}\\\tilde{v}_{dc}\end{bmatrix}$$

$$[\tilde{d}_{v1}]=[k_{i,v1}][\tilde{x}_{v1}]+[-k_{p,v1}k_d\ \ -k_{p,v1}]\begin{bmatrix}\tilde{i}_{dc}\\\tilde{v}_{dc}\end{bmatrix}$$

Voltage Controller; Boost mode

$$\frac{d}{dt}[\tilde{x}_{c1}]=[0][\tilde{x}_{c1}]+[-1][\tilde{i}_{dc}]$$

$$[\tilde{d}_{c1}]=[k_{i,c1}][\tilde{x}_{c1}]+[-k_{p,c1}][\tilde{i}_{dc}]$$

Current Controller; Boost mode

$$\frac{d}{dt}[\tilde{x}_{v2}]=[0][\tilde{x}_{v2}]+[-k_d\ \ -1]\begin{bmatrix}\tilde{i}_{dc}\\\tilde{v}_{dc}\end{bmatrix}$$

$$[\tilde{d}_{v2}]=[-k_{i,v2}][\tilde{x}_{v2}]+[k_{p,v2}k_d\ \ k_{p,v2}]\begin{bmatrix}\tilde{i}_{dc}\\\tilde{v}_{dc}\end{bmatrix}$$

Voltage Controller; Buck mode

$$\frac{d}{dt}[\tilde{x}_{c2}]=[0][\tilde{x}_{c2}]+[-1][\tilde{i}_{dc}]$$

$$[\tilde{d}_{c2}]=[-k_{i,c2}][\tilde{x}_{c2}]+[k_{p,c2}][\tilde{i}_{dc}]$$

Current Controller; Buck mode

Other components in the DC Microgrid

Fig. 4. The constructed small signal model of the studied system.

are parameters of the boost PI controller, and k_d is the droop resistance used for droop control in the microgrid. Similarly, when the voltage controller operates in the buck mode, the duty cycle d_{v2} can be calculated as follows:

$$\begin{cases}\dfrac{dx_{v2}}{dt}=v_{ref}-i_{dc}k_d-v_{dc}\\[6pt]d_{v2}=-\left[k_{p,v2}(v_{ref}-i_{dc}k_d-v_{dc})+k_{i,v2}x_{v2}\right]\end{cases}\tag{5}$$

where x_{v2} is the state variable of the buck PI controller, $k_{p,v2}$ and $k_{i,v2}$ are parameters of the buck PI controller. In the case of a current controller, as shown in Fig. 3, the operation mode depends on the value of the reference current. The current controller operates in the boost mode if the reference current is positive and in the buck mode if not. Similar to the voltage controller, the duty cycle of the current controller, d_{c1} and d_{c2}, can be calculated as follows:

$$\begin{cases}\dfrac{dx_{c1}}{dt}=i_{ref}-i_{dc}\\[6pt]d_{c1}=k_{p,c1}(i_{ref}-i_{dc})+k_{i,c1}x_{c1}\end{cases}\tag{6}$$

$$\begin{cases}\dfrac{dx_{c2}}{dt}=i_{ref}-i_{dc}\\[6pt]d_{c2}=-\left[k_{p,c2}(i_{ref}-i_{dc})+k_{i,c2}x_{c2}\right]\end{cases}\tag{7}$$

where x_{c1} and x_{c2} are the state variables of the boost PI controller and the buck PI controller, respectively. The reference current can be input directly or can be obtained by inputting the reference power and calculating $i_{ref}=P_{ref}/v_{dc}$ as shown in the dotted line portion of Fig. 2.

2.4. DC microgrid modeling

To study the dynamic behavior of the BESS in a common context, a generic DC microgrid modeling method, as proposed in [39], is used. For dynamic analysis, source components in DC microgrids are categorized into two types: the constant-power-and-resistive component and the voltage-controlled component. The constant-power-and-resistive component can be used to represent constant power sources, constant power loads, and constant resistive loads. The voltage-controlled component can be used to represent sources with voltage controllers. Additionally, a mathematical model for delivery lines in DC microgrids

is also derived, which can be expressed as:

$$\frac{di_{ij}}{dx}=\frac{1}{len_{ij}L_l}(v_i-v_j-i_{ij}len_{ij}R_l)\tag{8}$$

where len_{ij} is the length of the delivery line connecting buses i and j, i_{ij} is the current flow through the delivery line, and v_i and v_j are voltages at bus i and bus j, respectively. L_l and R_l are the unit inductance and the unit resistance of the delivery line, respectively. The detailed modeling process of other components can be found in the literature [39].

3. Small signal analysis

3.1. Methodology

The small signal analysis is a powerful tool for obtaining information on the stability and dynamics of a system around an operation point [40]. Eigenvalues or modes of a dynamic system are key results derived from a small signal analysis. The location of the eigenvalues obtained from the small signal model can indicate whether the system is stable at the operation point. Specifically, if at least one eigenvalue lies in the right half of the complex plane, the system is unstable. The imaginary and real parts of the eigenvalues provide additional information on the oscillation frequency and convergence speed of the system after experiencing a small disturbance, respectively. Furthermore, the participation factor is another result that can be obtained from the small signal analysis, which describes the relationship between modes and state variables in the small signal model. In the context of BESS, the identification of essential components for dominant modes is facilitated by determining the state variables associated with the highest participation factors for those modes.

To derive the small signal model of the studied system, the Taylor series linearization [41] is used. Firstly, it is required to introduce small signal disturbances to both the state variables and the algebraic variables of each component model, including (2), (3), (4), (5), (6), (7), and (8) as well as the constant-power-and-resistive component and the voltage-controlled component models.

$$\begin{cases}x=X+\tilde{x}\\u=U+\tilde{u}\end{cases}\tag{9}$$

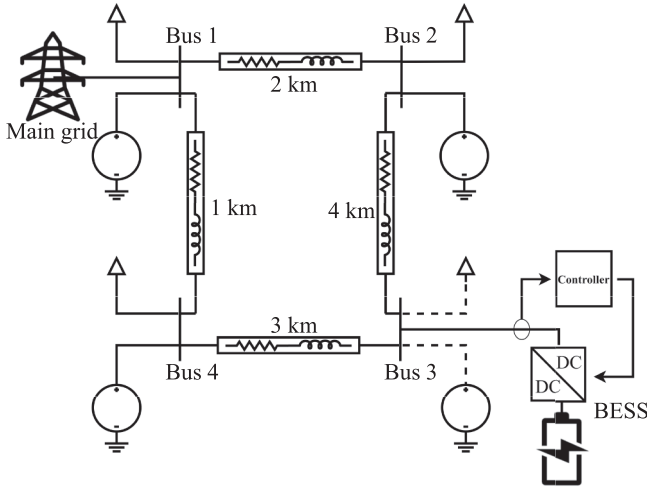After substituting (9) into each component model mentioned above,

Fig. 5. Investigated DC microgrid integrated with a BESS.

the steady-state and high-order terms in their Taylor series can be eliminated to obtain the small signal state space model.

$$\widetilde{x} = A\widetilde{x} + B\widetilde{u} \tag{10}$$

where matrix **A** is the system matrix, and matrix **B** is the input matrix. The constructed small signal model of the system is illustrated in the Fig. 4, where each box represents a sub-component of the system. In addition to the state variables of each sub-component, the input and output variables between different sub-components are also specified in the diagram. The state set of the entire studied system is $\mathbf{x} = [i_{R1}, i_{R2}, i_L, v_{dc}, x_v/x_c, i_{ij}, v_i, i_{ci}, v_{ci}]$. External inputs into the investigated system are only the current from the main grid i_{ui} and the battery bank open-circuit voltage OCV. Other input variables in each sub-component are output variables from another sub-components within the system, as shown in the Fig. 4. This small-signal model is easily implementable in various simulation software or programming languages; in this study, the MATLAB software was used. To get eigenvalues of the studied system matrix **A**, the following equation can be solved.

$$\det(A - \lambda I) = 0 \tag{11}$$

where **A** is an $n \times n$ matrix, λ is an $n \times 1$ eigenvalue vector. If there is a positive eigenvalue, the system will diverge if the system suffers a disturbance. In addition, even if there is no positive eigenvalue, the system dynamic response can be approximated by a superposition of n modes. However, the convergence time constant of some modes may be too small or too large to be relevant for the dynamic research timescale, so only some domain modes should be selected for eigenvalue analysis. The relationship between the kth mode and h^{th} state variable can be represented by the participation factor p_{hk}. For obtaining participation

factors, the right eigenvector ϕ_k and left eigenvector ψ_k need to be calculated as

$$\begin{cases} A\phi_k = \lambda_k \phi_k \\ \psi_k A = \lambda_k \psi_k \end{cases} \tag{12}$$

where the right eigenvector ϕ_k is an $n \times 1$ vector while the left eigenvector ψ_k is a $1 \times n$ vector. Then, the participation factor of the kth mode and h^{th} state variable is

$$p_{hk} = \phi_{hk}\psi_{kh} \tag{13}$$

3.2. Eigenvalues and participation factors analysis

Based on the models proposed in Section 2 and the methodology described in Section 3.1, small signal models of a DC microgrid equipped with BESSs were developed in the MATLAB/Simulink platform to explore the effects of the BESS on DC microgrid stability and dynamics. To facilitate this analysis, a modified generic DC microgrid with four buses at a rated voltage of 300 V was employed. The structure and parameters of the system were referenced from the configuration described in papers [39] and [42], with modifications made to better align with the research focus of this paper. The system structure is depicted in Fig. 5, and the default system parameters are listed in Table 3. Each bus is connected to a voltage-controlled source and a constant power load. Power interaction with the main grid only occurs at bus 1. Depending on research scenarios, the voltage-controlled source or constant power load at bus 3 was replaced with a V-BESS or a C-BESS. The eigenvalues of the studied system under five distinct scenarios were calculated, namely: (1) Without any BESS, (2) With a V-BESS in boost mode, (3) With a V-BESS in buck mode, (4) With a C-BESS in boost mode, and (5) With a C-BESS in buck mode. In the scenarios 3 and 4, P_3 was set at 4 kW. The resulting eigenvalues are summarized in Table 4, and their corresponding participation factors are presented in Fig. 6.

Compared to the initial DC microgrid without any BESS, four new eigenvalues are introduced to the system due to the introduction of V-BESS and C-BESS. In scenario 1, system eigenvalues can be readily classified into three classifications: (1) Non-oscillation modes with small real parts ($\lambda_{1\sim4}$), (2) High-frequency oscillation modes ($\lambda_{5\sim12}$), and (3) Non-oscillation modes with real parts greater than -500 ($\lambda_{13\sim16}$). According to the participation factor analysis results depicted in Fig. 6, the biggest participation factors of modes $\lambda_{1\sim4}$ are state variables $v_1 \sim v_4$, regulated by voltage-controlled sources at each bus. Hence, the primary contributing components for modes $\lambda_{1\sim4}$ are the voltage-controlled sources at each bus. Considering that the main participation factors for high-frequency modes $\lambda_{5\sim12}$ are the currents and voltages of constant power loads, it follows that constant power loads constitute the main contributing components for modes $\lambda_{5\sim12}$. The main participation factors for modes $\lambda_{13\sim16}$ are the currents on delivery lines. Thus, the primary contributing components for these modes are the delivery lines in the DC microgrid. The V-BESS at bus 3 introduces an oscillating mode

Table 3
Default parameters of the studied system.

Parameter	Value	Parameter	Value	Parameter	Value	Parameter	Value
V_{rated} (V)	300.0000	l_1 (H)	0.0002	P_2 (kW)	−3.0000	$R_{2,cell}$ (Ω)	0.0492
c_{G1} (F)	0.0010	l_2 (H)	0.0002	P_3 (kW)	−4.0000	$R_{b,cell}$ (Ω)	0.1975
c_{G2} (F)	0.0030	l_3 (H)	0.0002	P_4 (kW)	−3.0000	L_f (H)	0.0033
c_{G3} (F)	0.0030	l_4 (H)	0.0002	L_l (H/km)	0.5480	R_f (Ω)	0.0835
c_{G4} (F)	0.0060	c_1 (F)	0.0002	R_l (Ω/km)	0.0990	C_{dclink} (F)	0.0200
k_1 (Ω)	0.0500	c_2 (F)	0.0002	len_{12}	2.0000	$k_{p,v1}$	0.0150
k_2 (Ω)	0.0500	c_3 (F)	0.0003	len_{23}	4.0000	$k_{i,v1}$	0.0900
k_3 (Ω)	0.0500	c_4 (F)	0.0003	len_{34}	3.0000	$k_{p,v2}$	0.1000
k_4 (Ω)	0.0500	r_1 (Ω)	∞	len_{41}	1.0000	$k_{i,v2}$	0.6000
r_{p1} (Ω)	0.0400	r_2 (Ω)	∞	OCV_{cell} (V)	3.3000	$k_{p,c1}$	0.0030
r_{p2} (Ω)	0.0400	r_3 (Ω)	∞	$\tau_{1,cell}$ (s)	25.8897	$k_{i,c1}$	0.0500
r_{p3} (Ω)	0.0400	r_4 (Ω)	∞	$R_{1,cell}$ (Ω)	0.0254	$k_{p,c2}$	0.0030
r_{p4} (Ω)	0.0400	P_1 (kW)	−4.0000	$\tau_{2,cell}$ (s)	4931.6000	$k_{i,c2}$	0.0500

Table 4
Eigenvalues of five studied scenarios.

Eigenvalue	Without any BESS	With a V-BESS in boost mode	With a V-BESS in buck mode	With a C-BESS in boost mode	With a C-BESS in buck mode
λ_1	−19617.5119	−19617.5119	−19617.5119	−19617.5119	−19617.5119
λ_2	−6448.1811	−6426.7098	−6426.7112	−6426.7114	−6426.7103
λ_3	−6397.9453			−760.5173	−762.0896
λ_4	−3085.8512	−3086.7525	−3086.7572	−3086.7859	−3086.7840
$\lambda_{5,6}$	−110.1512 ± 5015.9511	−110.1512 ± 5015.9511	−110.1886 ± 5015.9537	−110.1886 ± 5015.9537	−110.1512 ± 5015.9511
$\lambda_{7,8}$	−100.2083 ± 5054.4023	−100.2083 ± 5054.4036	−100.2672 ± 5054.4075	−100.2671 ± 5054.4075	−100.2083 ± 5054.4036
$\lambda_{9,10}$	−121.2285 ± 4131.0737	−25.9575 ± 4131.0737	−172.0743 ± 4113.3053		
$\lambda_{11,12}$	−97.6658 ± 4140.5309	−97.6756 ± 4140.5333	−97.7202 ± 4140.5358	−97.7199 ± 4140.5359	−97.6754 ± 4140.5329
λ_{13}	−267.4952	−267.3181	−267.3176	−267.4237	−267.3818
λ_{14}	−180.6569	−180.6569	−180.6569	−180.6569	−180.6569
λ_{15}	−250.1336	−169.1988	−267.3176	−248.3995	−244.9604
λ_{16}	−432.1540	−424.8606	−424.7571	−442.9208	−442.2814
$\lambda_{17,18}$		−38.5240 ± 338.7695	−49.8401 ± 344.5634		
λ_{19}		−4.4350	−4.4546	−13.4391	−13.5352
λ_{20}		−0.0386	−0.0386	−0.0386	−0.0387
λ_{21}		-2.2025×10^{-4}	-2.0301×10^{-4}	-2.0242×10^{-4}	-2.0310×10^{-4}
λ_{22}				−338.1419	−326.9819
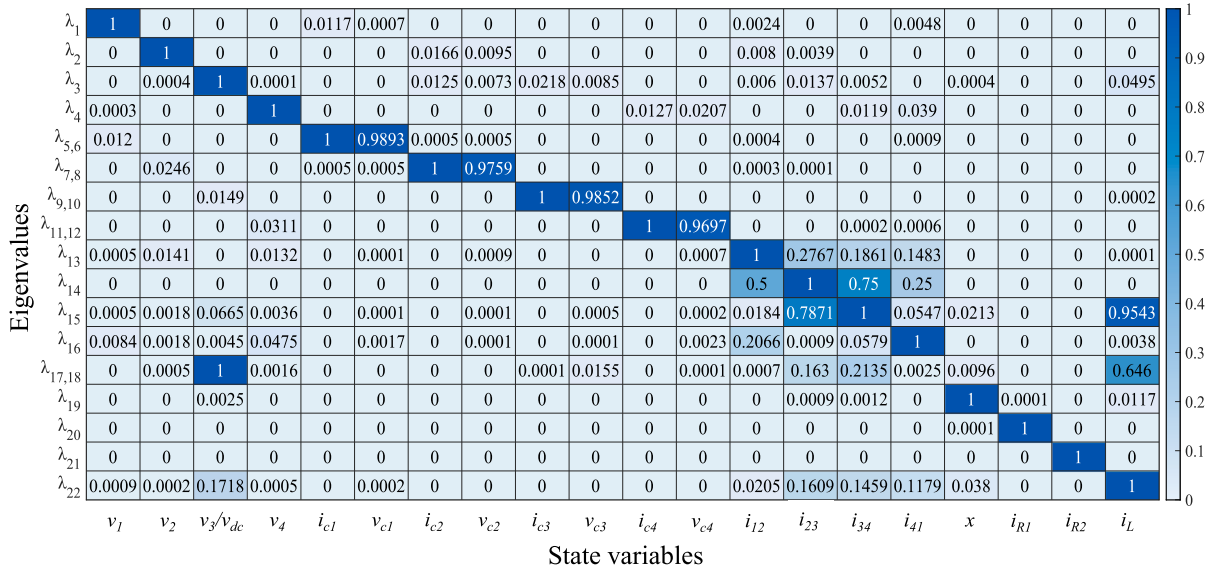
Fig. 6. Participation factors of the system eigenvalues.

($\lambda_{17,18}$) and three additional non-oscillating modes (λ_{19}, λ_{20}, and λ_{21}). On the other hand, the C-BESS does not introduce the $\lambda_{17,18}$ mode but instead introduces a new non-oscillation mode λ_{22} with a time constant of approximately 0.003 s.

The effects of the BESS on the dynamic behavior and stability of a DC microgrid are mainly reflected in mode λ_{15} and modes $\lambda_{17,18}$ to λ_{22}. Due to the relatively high participation factors of v_{dc} and i_L associated with mode λ_{15}, the delivery line has a complex interaction with the DC bus capacitor and the filter inductor within the BESS. The dominant oscillation mode in a DC microgrid with a V-BESS is $\lambda_{17,18}$. The introduction of mode λ_{19} is attributed to the BESS controllers, given its significant participation factors associated with the state variable x of the controller. Mode λ_{19} is characterized by a time constant ranging approximately from 0.05 s to 0.25 s. In addition, the mode λ_{22} is exclusively induced by the C-BESS. According to the participation factor analysis, both mode $\lambda_{17,18}$ and mode λ_{22} have relative high participation factors of v_{dc}, i_L, and delivery line current. Therefore, these two modes are affected not only by the DC bus capacitor and the filter inductor in the BESS but also by the delivery lines. Although modes λ_{20} and λ_{21} are also introduced by the BESS, their time constants depend only on the time constants of the battery bank RC pairs. Moreover, the time constants of modes λ_{20} and λ_{21} are over the time scale of system dynamic research. In summary, the interaction within the BESS occurs primarily between the DC bus capacitor and the filter inductor, while the delivery line is the main component with which the BESS interacts in the DC microgrid. Notably, the number of eigenvalues remains unchanged in boost mode and buck mode, regardless of whether it is a V-BESS or C-BESS. Consequently, the following study in this section will focus on analyzing the BESSs in boost mode.

3.3. Sensitivity analysis

This subsection aims to analyze the effect of system parameter variations on eigenvalue modes in consideration of converter configuration, controller parameters, battery bank configuration, and delivery line length. By examining the primary state variables identified earlier, the sensitivity analysis can determine the critical system parameters affecting BESS dynamic modeling. The sensitivity analysis can not only guide the design of an appropriate BESS in a DC microgrid but also reflect the parameter variations impact due to aging during the operation stage. In each eigenvalue locus in the sensitivity analysis, only one parameter changes while other system parameters remain at their default setting. In the following, this study uses the analysis of the V-BESS to illustrate the sensitivity analysis, while the sensitivity analysis results of the C-BESS are presented in Appendix I, following a similar process as the V-BESS case. The difference between the boost mode and
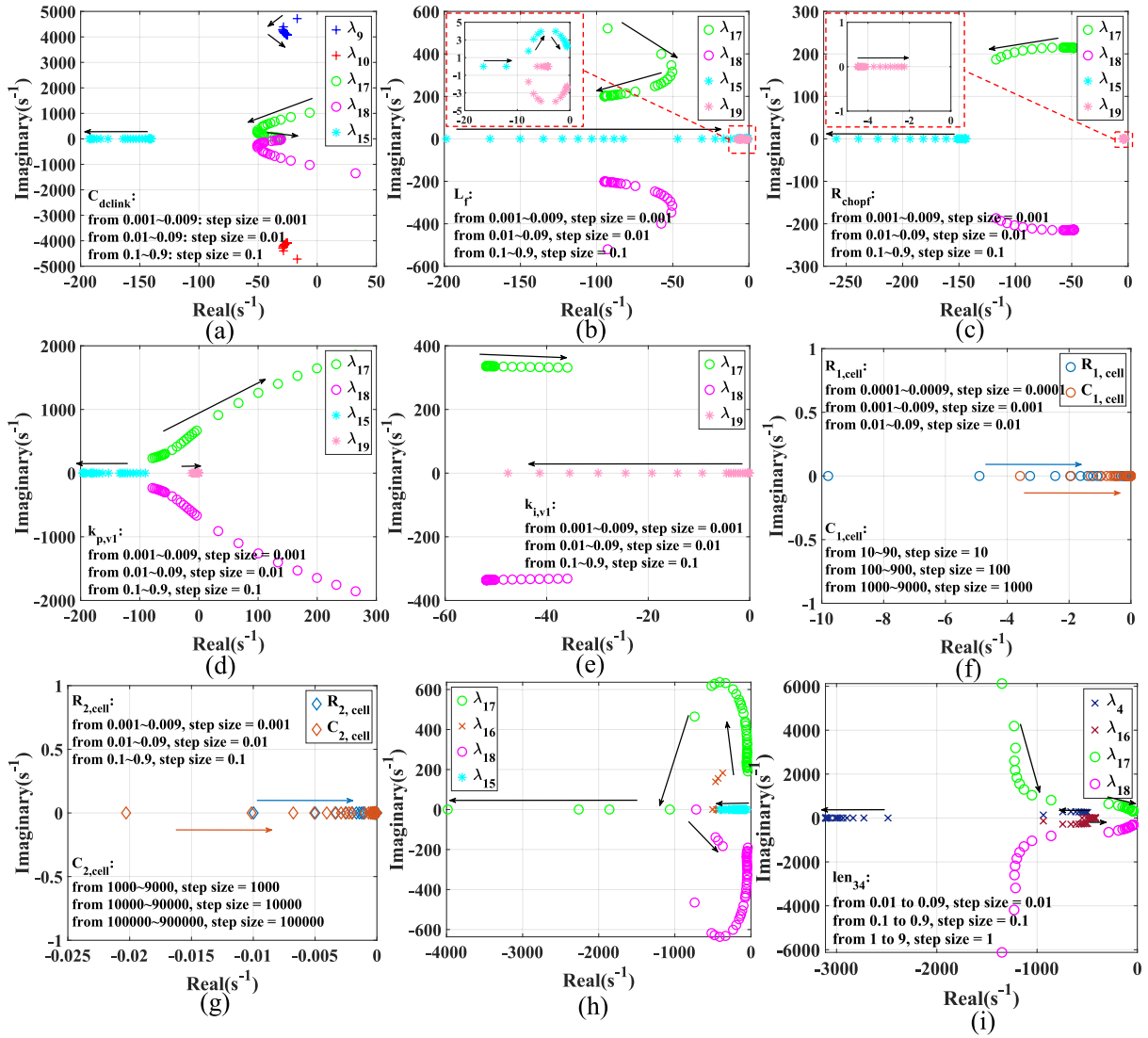
Fig. 7. Eigenvalue loci of system parameter variations (V-BESS): (a) DC bus capacitance C_{dclink}, (b) Filter inductance L_f; (c) Filter resistance R_f; (d) Controller parameter $k_{p,v1}$, (e) Controller parameter $k_{i,v1}$, (f) Battery bank RC pair 1, (g) Battery bank RC pair 2, (h) Cells connection number m and n, (i) Delivery line 34 length len_{34}.

the buck mode is reflected by changing the load at bus 3.

The parameters of the BBBC studied here are the DC bus capacitance C_{dclink}, the filter inductance L_f and its parasitic resistance R_f. C_{dclink} and L_f are commonly selected based on the demand for ripple limitation on both sides of the BBBC, while the value of R_f is determined by the manufacturing technology and aging status of the filter inductor. Results of the sensitivity analysis of these three parameters are shown from Fig. 7 (a) to (c). An increase in C_{dclink} capacity from 0.001 to 0.9 causes a decrease in the oscillation frequency of mode $\lambda_{17,18}$ from 216.7032 Hz to 5.3172 Hz while the damping ratio increases initially and then decreases. A small C_{dclink} capacity results in a positive damping ratio, leading to system instability. The damping ratio reaches its largest value when the C_{dclink} capacity is 0.03F. In the case of L_{chopf}, an increase to 80 mH causes non-oscillation modes λ_{15} and λ_{19} to become an oscillation mode with a low damping ratio and a small frequency. As shown in Fig. 7 (c), when the R_f varies within 0.1, the impact on the transient behavior of the system is negligible, while the increase of the R_f with a step size of 0.1 can increase the damping ratio of the system. Therefore, when selecting C_{dclink} and L_f capacity, the transient behavior of the system should also be considered in addition to the ripple to obtain a better performance. However, it is not recommended to increase system

damping by increasing R_f due to its inefficiency.

In the boost mode of the V-BESS, a conventional PI controller is employed, which has two parameters: $k_{p,v1}$ and $k_{i,v1}$. The eigenvalue loci of these two parameters are illustrated in Fig. 7 (f) and Fig. 7 (e), respectively. The controller parameter $k_{p,v1}$ has a significant impact on system stability. When the value of the controller parameter $k_{p,v1}$ is approximately 0.07, the eigenvalue $\lambda_{17,18}$ moves across the imaginary axis to the right half-panel, leading to system instability. For $k_{i,v1}$, the damping ratio of mode $\lambda_{17,18}$ is reduced when the value is increased. Therefore, it is crucial to carefully select a suitable value for $k_{p,v1}$ to maintain system stability.

The battery bank configuration parameters include the values of RC pairs, cell connection within the battery bank, and the OCV_{cell}. Sensitivity analysis results for RC pair values and cell connection are presented in Fig. 7 (f) to (h), while OCV_{cell} is not shown here due to its insignificant effect. The mode λ_{20} is only affected by $R_{1,cell}$ and $C_{1,cell}$, while the mode λ_{21} is only affected by $R_{2,cell}$ and $C_{2,cell}$. Furthermore, it was observed that the amplitude decay time-constant of mode λ_{20} is equal to the time-constant of the RC pair 1 ($|\sigma_{20}| = R_{1,cell}C_{1,cell}$) and the amplitude decay time constant of mode λ_{21} is equal to the time-constant of the RC pair 2 ($|\sigma_{21}| = R_{2,cell}C_{2,cell}$). Therefore, increasing $R_{1,cell}$, $C_{1,cell}$,
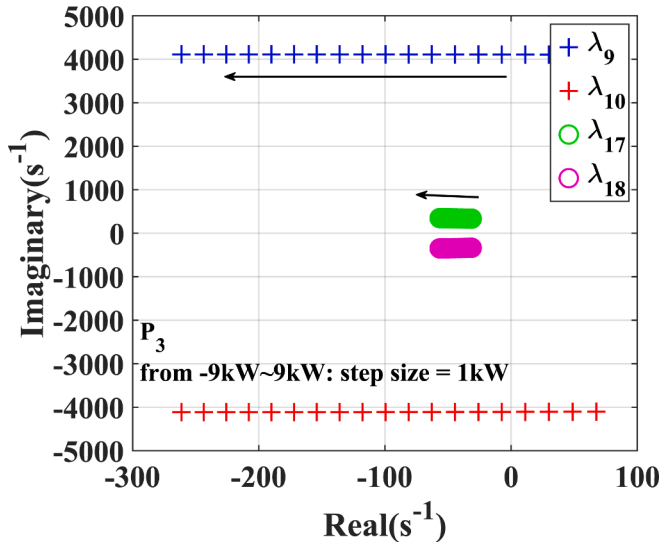
Fig. 8. Eigenvalue locus of P_3.

$R_{2,cell}$, and $C_{2,cell}$ can move eigenvalue λ_{20} or eigenvalue λ_{21} to the right, but this will never cause system instability. To study the effect of cell connection within the battery bank, the total number of cells was kept constant at 10800, and then the number of cells in series m and the number of cells in parallel n were gradually increased and decreased from $m = 12$ and $n = 900$ to $m = 900$ and $n = 12$. Within a reasonable range, the frequency and damping ratio of the mode $\lambda_{17,18}$ increase when the number of cells in series m increases. Therefore, when designing the cell connection, increasing the number of series connections m can improve the performance of system dynamic response and stability.

The participation analysis revealed that the BESS interacts with the delivery line, prompting a closer examination of the line length. The participation analysis revealed that the BESS interacts with the delivery line, prompting a closer examination of the line's length. As the sensitivity analysis result illustrated in Fig. 7 (i), it can be seen that the longer the delivery line len_{34} is, the lower damping ratio of the complex mode $\lambda_{17,18}$ has. On the other hand, when the length of line 34 is smaller or equal to 0.1 km, the eigenvalue λ_4 and λ_{16} forms an oscillation mode with a high frequency of over 74.8408 Hz.

The eigenvalue analysis shows that the number of modes in the system remains the same when the BESS changes between the buck mode and boost mode. The eigenvalue locus in Fig. 8 reveals that the change of operation modes only affects the location of eigenvalues but not the number. Furthermore, whether in buck mode or boost mode, the eigenvalue locus exhibits a consistent tendency towards changes when there is an increase or decrease in power P_3. Specifically, as P_3 gradually increases from -9 kW to 9 kW, both the high-frequency oscillation mode $\lambda_{9,10}$ and the low-frequency oscillation mode $\lambda_{17,18}$ move to the left. It is

worth noting that a high load at bus 3 can cause the system to become unstable due to the divergent high-frequency oscillation, while the high charging power of the BESS does not have a similar limitation.

4. Real-time software-in-the-loop simulation results and discussions

A real-time software-in-the-loop simulation model, as illustrated in Fig. 9, was employed to validate both small signal and sensitivity analyses. Furthermore, this paper proposes suitable models of V-BESS and C-BESS in a DC microgrid for dynamic studies. These models are compared through the real-time software-in-the-loop simulation. A fully detailed electromagnetic model is firstly developed in the MATLB 2021b platform. The investigated DC microgrid configuration remains consistent with Fig. 5 and Table 3. Both its electromagnetic characteristics and switching dynamics are also considered. The simulation model is transferred to C code through the RT-Lab tool and executes on a real-time simulator, OPAL RT 5707XH, with a time step of ten microsecond. During the real-time simulation, the host computer sends real-time control signals, such as disturbances, to the OPAL RT 5707XH through the RT-Lab interface. Subsequently, the OPAL RT 5707XH returns the output results to the host computer. During these communication processes, a unit time delay is considered.

4.1. Validation of the small signal analysis and sensitivity analysis

Seven cases were designed to examine the results of previous analyses. The first case aims to compare the dynamic behaviors of a DC microgrid without any BESS, a DC microgrid with a V-BESS, and a DC microgrid with a C-BESS. cases 2 ~ 7 were designed to test the effect of C_{dclink}, L_f, $k_{p,v1}$, cell connection, line length len_{34}, and P_3 in a DC microgrid equipped with a V-BESS. Except for the case of $k_{p,v1}$ and P_3, all

Table 5
The designing of studied cases.

| Studied cases	Comparison	Disturbance	Result
Case 1	No BESS, V-BESS, and C-BESS	A step load change at 0.5 s from −4 kW to −6 kW	Fig. 10 (a)
Case 2	Different C_{dclink} values	A step load change at 0.5 s from −4 kW to −6 kW	Fig. 10 (b)
Case 3	Different L_f values	A step load change at 0.5 s from −4 kW to −6 kW	Fig. 10 (c) and Fig. 11
Case 4	Different $k_{p,v1}$ values	$k_{p,v1}$: 0.01 → 0.05 → 0.1	Fig. 10 (d)
Case 5	Different cell connections	A step load change at 0.5 s from −4 kW to −6 kW	Fig. 10 (e)
Case 6	Different line lengths	A step load change at 0.5 s from −4 kW to −6 kW	Fig. 10 (f)
Case 7	Different P_3 values	P_3: 8 kW → 3 kW → -3 kW → -8 kW	Fig. 12 (a) and Fig. 12 (b)
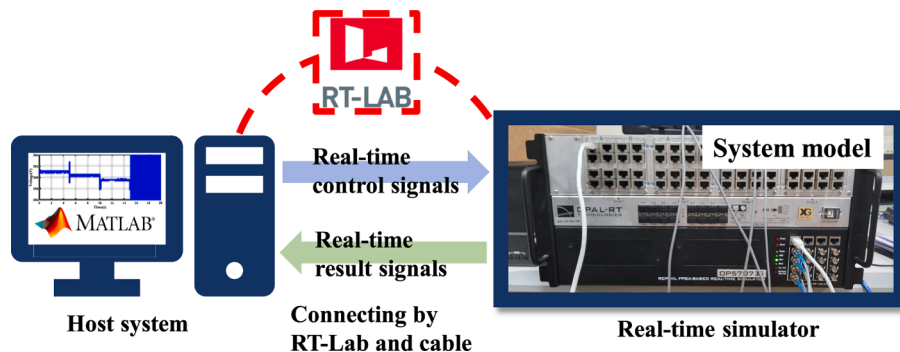
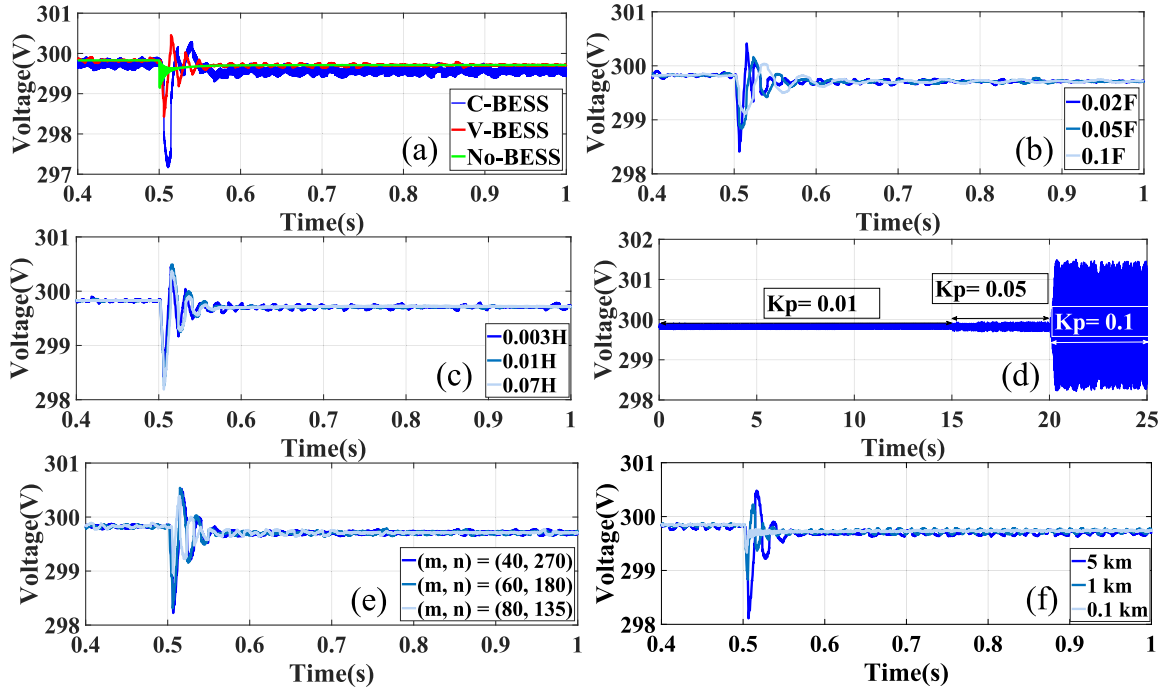**Fig. 9.** Real-time simulation environment with OPAL-RT 5707XH.

Fig. 10. Bus 3 voltage on different scenarios: (a) Scenario 1, (b) Scenario of C_{dclink}, (c) Scenario of L_f, (d) Scenario of $k_{p,v1}$, (e) Scenario of cells connection, (f) Scenario of len_{34}.

other cases introduced a disturbance at 0.5 s, which increased the P_3 from −4 kW to −6 kW. In the case of $k_{p,v1}$, other parameters remained constant while the $k_{p,v1}$ was increased from 0.01 to 0.05 and then to 0.1. In the case of P_3, the P_3 was first decreased from 8 kW to 3 kW, then further decreased to −3 kW, causing the BESS to transition from a charging status to a discharging status. Finally, the P_3 was further decreased from −3 kW to −8 kW. A summary of designed cases is listed in Table 5.

The experiment result of case 1 is shown in Fig. 10 (a). In this experiment, the voltage-controlled source and the constant power load at bus 3 were replaced with a V-BESS and a C-BESS, respectively. From Fig. 10 (a), it can be seen that the oscillation frequency of the DC microgrid without BESS is around 648 Hz, indicating that the dominant oscillation mode is $\lambda_{9,10}$. However, due to their low damping ratio, it can also be found that non-oscillation modes play important roles in the DC microgrid without a BESS. In comparison, the DC microgrid equipped with a V-BESS displayed a low-frequency mode at 37 Hz due to the introduced mode $\lambda_{17,18}$. In the case of the DC microgrid equipped with a C-BESS, because there is no introduced oscillation mode, the dominant mode is still the non-oscillation mode with a longer response time. These findings demonstrate that the presence of a BESS in a DC microgrid has a significant impact on the dynamic behaviors of the system. Therefore, the BESS modeling should be considered for an accurate analysis.

The goal of case 2 is to verify the impact of C_{dclink} capacitance on the dynamic behaviors of the system. The result presented in Fig. 10 (b) demonstrates that increasing the C_{dclink} capacitance leads to an increase in the frequency of the dominant oscillation mode. In this scenario, the C_{dclink} capacitance increased from 0.02F to 0.05F, then to 0.1F. In the small signal analysis, it was observed that the system with a 0.02F C_{dclink} exhibited the smallest real part value of the eigenvalue $\lambda_{17,18}$, which is reflected in the real-time simulation as the fastest convergence speed. As the capacity of the C_{dclink} increases from 0.02F to 0.1F, the oscillation frequency in the real-time simulation also decreases gradually from 37 Hz to 14 Hz. This decrease in frequency is consistent with the eigenvalue analysis, where the imaginary part of the dominant eigenvalues decreases gradually. The findings from this scenario suggest that selecting an appropriate C_{dclink} capacitance is crucial for improving the transient performance of the system.
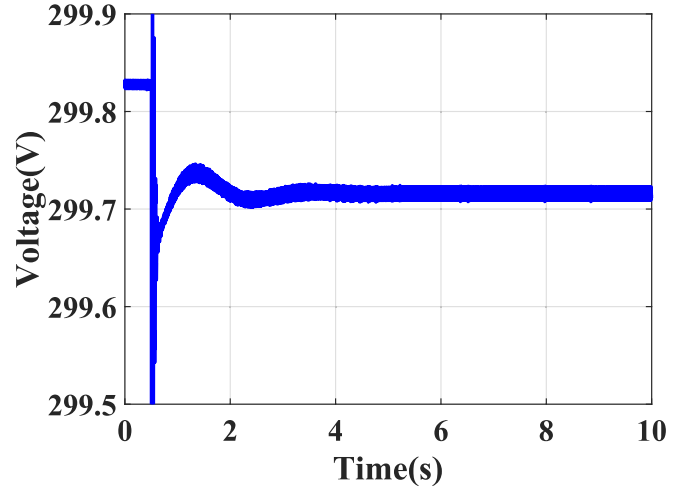

Fig. 11. Experiment result of a V-BESS equipped with a 0.2H L_f.

performance of the system.

The result of case 3 confirms that increasing the L_f capacity from 0.003H to 0.07H can increase the convergence speed with little impact on the oscillation frequency. This finding is consistent with the small signal analysis, which shows that the dominant oscillation mode $\lambda_{17,18}$ moves to the left but not up and down. However, this increase in convergence speed comes at the cost of an amplified overshoot response due to the rapid shift of the non-oscillation mode λ_{15} to the right. An additional experiment was conducted with an L_f of 0.2H to verify that a large capacity of L_f will change the non-oscillation modes λ_{15} and λ_{19} to a low-frequency oscillation mode. As shown in Fig. 11, the new oscillation mode has a relatively low frequency of around 0.43 Hz. Therefore, for better performance, one should choose a proper capacity of L_f, considered the convergence speed and overshoot comprehensively.

Case 4 is one of the critical cases in the small signal analysis. The increase in $k_{p,v1}$ can cause the system eigenvalues $\lambda_{17,18}$ cross the
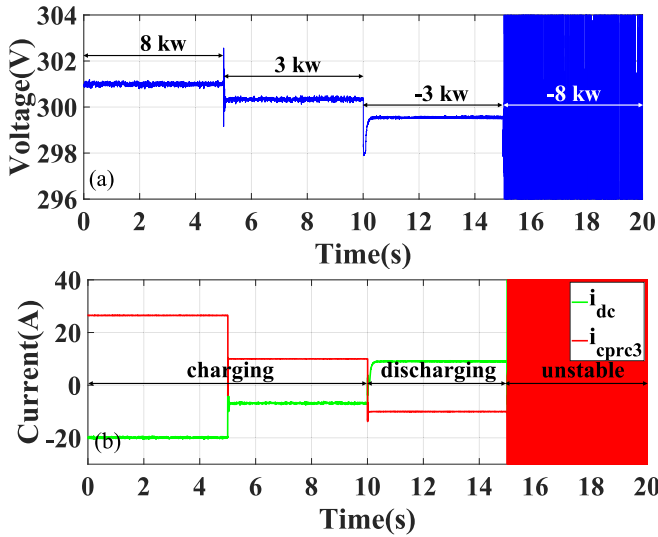
Fig. 12. Experiment results of changing the P_3: (a) Bus 3 voltage, (b) Exporting currents of the BESS and the constant-power-resistive component at bus 3.

imaginary axis. This will cause the system from stable to unstable or oscillatory. Therefore, in the case 4, the stability of the system was tested with different values of $k_{p,v1}$, namely 0.01, 0.05, and 0.1. The controller parameter $k_{p,v1}$ was increased from 0.01 to 0.05 at 15 s, and then further increased to 0.1 at 20 s. Fig. 10 (d) presents a consistent result with Fig. 7 (d), indicating that the system becomes unstable as $k_{p,v1}$ increases to 0.1. $k_{p,v1}$ determines the strength of the proportional action in response to the error between the reference voltage and the actual voltage. Excessive responses can induce oscillatory behavior, as the controller may produce an unregulated overshooting correction. Therefore, using an more appropriate $k_{p,v1}$ can enhance the stability of the system. Real-time experiments were conducted to investigate the impact of parameters such as $k_{i,v1}$. However, the results for R_f, OCV_{cell}, and RC-pairs parameters are not presented herein due to their negligible effects.

In case 5, the effect of the cell connection structure on the system's dynamic behaviors was investigated. The experiment involved increasing the number of cells in series m from 40 to 80 in increments of 20 while decreasing the number of cells in parallel n from 270 to 135 to maintain a constant total number of battery cells. The results of scenario 5 are shown in Fig. 10 (e). As the number of cells in series m increases, the frequency of the dominant oscillation mode of the system increases slightly from 34 Hz to 35 Hz and then to 37 Hz. The damping ratio has significantly increased, and the system with a larger m will converge
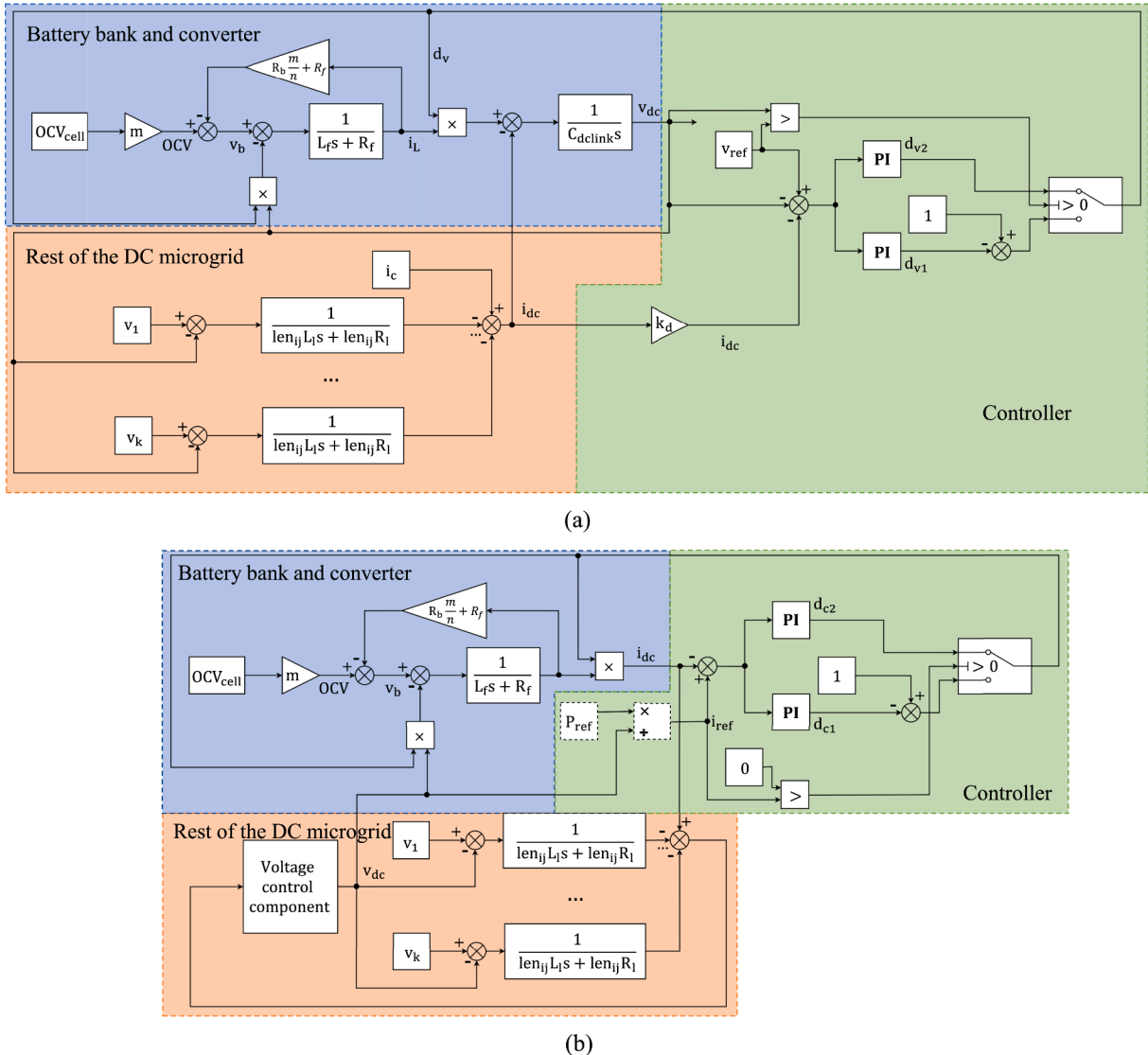
Fig. 13. Block diagram of the proposed dynamic models: (a) V-BESS model in a DC microgrid; (b) C-BESS model in a DC microgrid.
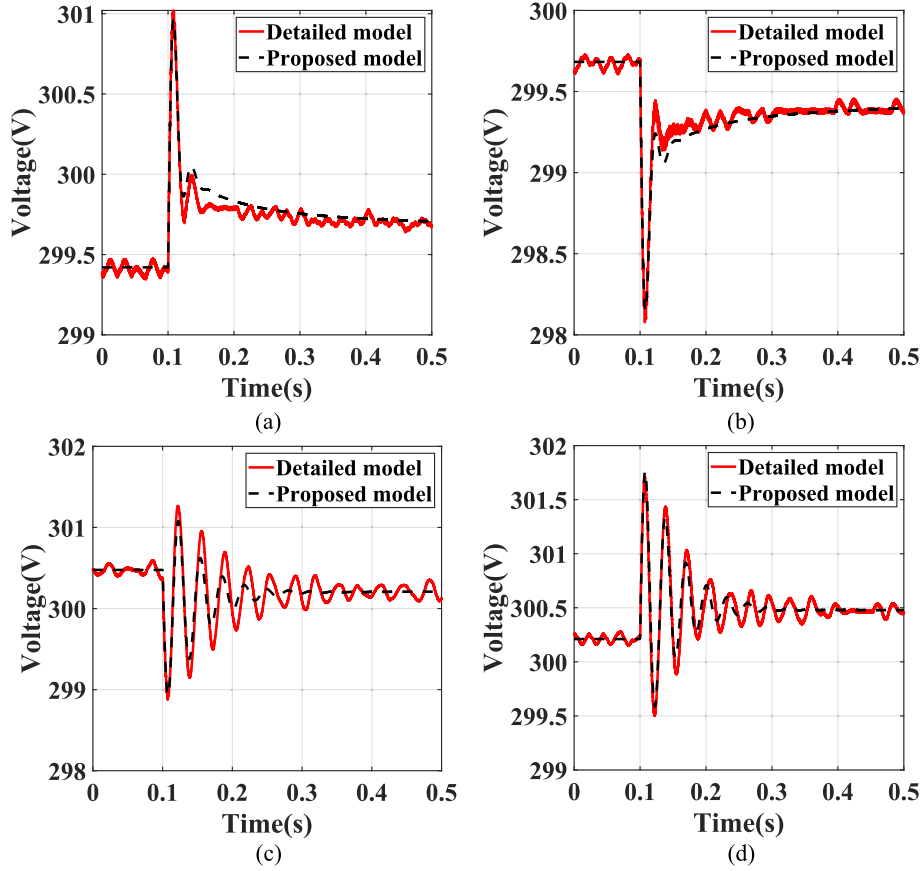
Fig. 14. Comparison of the detailed electromagnetic model and the proposed V-BESS model: (a) Load demand at bus 3 changes from −4 kw to −2 kw; (b) Load demand at bus 3 changes from −2 kw to −4 kw; (c) Source power at bus 3 changes from 4 kw to 2 kw; (d) Source power at bus 3 changes from 2 kw to 4 kw.

more quickly. These experimental findings are also consistent with the small signal analysis results. As shown in Fig. 7 (h), increasing the number of series m moves the eigenvalue $\lambda_{17,18}$ to the upper right. From the perspective of the battery bank port, changing the number of cells in series and parallel will change the port voltage, current, and the equivalent series resistance value without changing the recovery time constant of the port.

Real-time simulations also demonstrated the critical importance of considering the delivery line model in the dynamic analysis of a DC microgrid that is equipped with a BESS. In the case 6, the delivery line connecting the bus 3 and the bus 4 was increased from 0.1 km to 1 km and then to 5 km. The result shown in Fig. 10 (f) indicates that when the line length is as short as 0.1 km, the dominant mode of the system is the high-frequency oscillation mode. However, when the length of the delivery line is increased to 1 km, the dominant mode of the system becomes the mode $\lambda_{17,18}$. Further increasing the length of the delivery line to 5 km results in a decrease in the oscillation frequency of the system from 54 Hz to 32 Hz, and the damping ratio also decreases. These findings verify that although the oscillation mode $\lambda_{17,18}$ is introduced by the V-BESS, it is also sensitive to the delivery line and, therefore, should be considered in the dynamic study.

Case 7 was designed to test the effect of P_3 on the system. Because the case 7 is the other critical case identified from the small signal analysis. P_3 was changed during the system operation to study the system stability. When P_3 is positive, the constant-power-resistive component at bus 3 acts as a constant power source, while it behaves as a constant load when P_3 is negative. The result is consistent with the eigenvalue locus shown in Fig. 8. The increasing loads can reduce stability margins of the system and increase the system susceptibility to the small signal instabilities. The system finally becomes unstable when the V-BESS is expected to export excessive power. As depicted in Fig. 12, the system

becomes unstable when the load at bus 3 increases from −3 kW to −8 kW at 15 s. Moreover, the instability in this case can only be alleviated by reducing the load, because other parameters have little influence on $\lambda_{9,10}$. At 10 s, a voltage drop occurs at bus 3 due to the converter switching from the buck mode to the boost mode. It is worth noting that due to the droop control method employed in this DC microgrid, i_{dc} is not always complementary to i_{cprc3}. In summary, there is a significant limit to the V-BESS's discharging power compared to its charging power.

4.2. Proposed models

This subsection proposes suitable models of the V-BESS and the C-BESS in a DC microgrid for the dynamic study, which can capture the dominant behavior of BESSs while needing relatively low computational demands. To facilitate the easy application of BESS models to the dynamic study in a DC microgrid, this study proposes the frequency-domain models in Fig. 13. After comprehensive consideration of small signal analysis results and real-time simulation verification, this study proposes dynamic models which consist of three parts: the battery bank and converter, the controller, and the rest of the DC microgrid. In the battery bank and converter part of V-BESS, the effect of C_{dclink}, inductor filter, and cell series connection are considered, while in the C-BESS, the effect of C_{dclink} is considered in the voltage control component. In both of V-BESS and C-BESS, this study neglects the dynamics of the RC pairs in the system-level study and considers the voltage drop caused by the battery bank resistance and the filter resistance together. In the controller part, the PWM generator is omitted, and then the controller is directly connected to the converter through the duty cycle d. Moreover, for studies related to controller design and performance tests, this part of the model can be effortlessly replaced with the desired controller. As the significant effect of the delivery lines, they are considered in the rest of
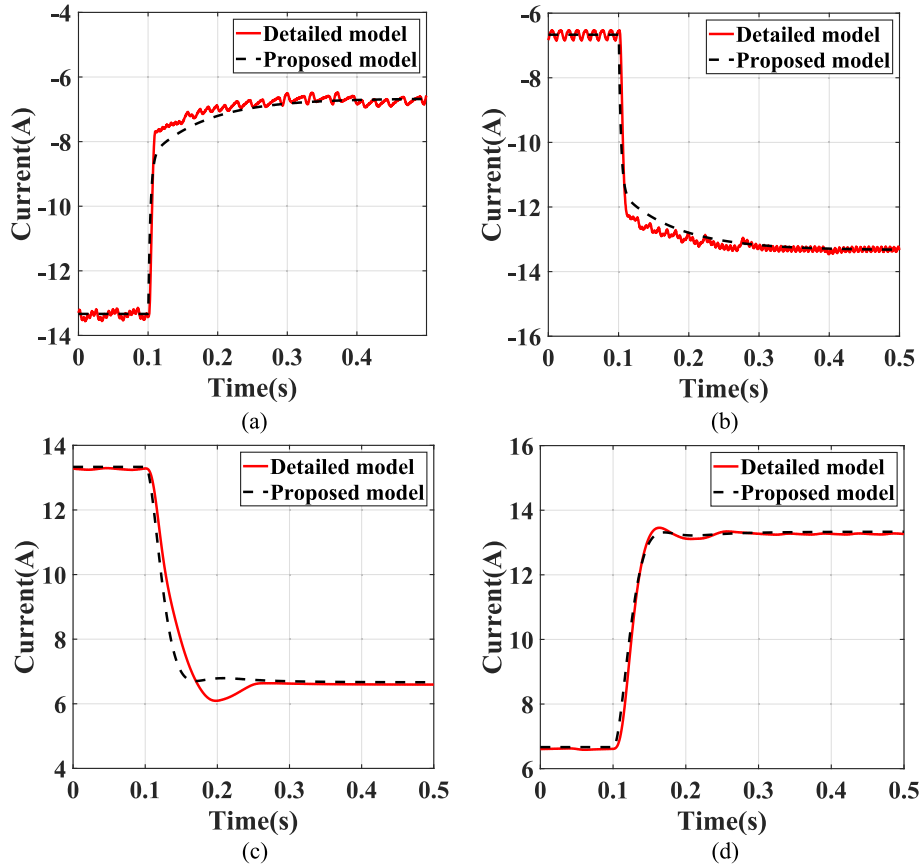
Fig. 15. Comparison of the detailed electromagnetic model and the proposed C-BESS model: (a) Reference power of the C-BESS changes from −4 kw to −2 kw, (b) Reference power of the C-BESS changes from −2 kw to −4 kw, (c) Reference power of the C-BESS changes from 4 kw to 2 kw; (d) Reference power of the C-BESS changes from 2 kw to 4 kw.

the DC microgrid part. The voltages of other buses connected to the bus where the BESS is located are represented by v_1 to v_k.

The proposed models were developed in MATLAB Simulink to compare their performance against the detailed electromagnetic model built in this section. Four scenarios were designed for each dynamic model to conduct a complete comparison. For a V-BESS in a DC microgrid, the first two scenarios are that the V-BESS works in the discharging mode while load demand at the bus 3 changes from −4 kw to −2 kw and from −2 kw to −4 kw, respectively. In the latter two scenarios, the V-BESS works in the charging mode while source power at bus 3 changes from 4 kw to 2 kw and from 2 kw to 4 kw, respectively. Results of the V-BESS are shown in Fig. 14 (a). For a C-BESS in a DC microgrid, the variable that was changed is the reference power of the C-BESS. In contrast, the values that were changed in the four scenarios remain consistent with those in the case of V-BESS. Results of C-BESS are shown in Fig. 15. The models proposed in this paper can capture the main dynamical behaviors of BESSs, particularly the maximum overshoot and convergence time of the transient process. Compared to the detailed electromagnetic model, the proposed model can significantly reduce the computational demand and modeling difficulty needed for its application. Using the same real-time computing device as for the detailed electromagnetic models, the minimum step size is 1.5 microseconds. The proposed models can reduce computational requirements by approximately 85 % without losing critical system information.

5. Conclusions

This paper presented the interaction mechanism of a V-BESS or a C-BESS in a DC microgrid through comprehensive small signal and sensitivity analyses. Through the eigenvalue and participation factors

analyses, this study found that the interaction within the BESS occurs primarily between the DC bus capacitor and the filter inductor, while the delivery line is the main component with which the BESS interacts in the DC microgrid. This study also identified critical component parameters: the DC bus capacitance C_{dclink}, the filter inductance L_f, controller parameters, the delivery line length, and cell connection within the battery bank. The effects of parameter variations were also analyzed through sensitivity analysis, and the results were verified through real-time software-in-the-loop simulations using an OPAL RT 5707XH. In addition, this paper demonstrated that for studying the dynamic behaviors of a BESS in a DC microgrid, the battery bank model only needs to consider the internal resistance and open-circuit voltage, rather than a full 2nd-order Thevenin model. The analysis results provided valuable insight and guidelines for BESS design and operation in a DC microgrid.

This paper also proposed dynamic models for both V-BESS and C-BESS integrated with a DC microgrid, capturing dominant behaviors with relatively low computation demands. Based on the results of small signal and sensitivity analyses, the models include all critical variables and parameters and, therefore, have great accuracy compared to the detailed electromagnetic model in all possible operation modes, particularly the transient process's maximum overshoot and convergence time. However, the computation cost can be reduced by approximately 85 % compared to the detailed electromagnetic model. Moreover, the proposed models have strong application extensibility due to their sub-modularity. While this study focused on particular DC microgrids and controllers, the examination of more intricate control loops and grid systems is reserved for subsequent research endeavors. To evaluate its controller, one can replace its sub-module in the model. For comparing BESS performance in diverse DC microgrid environments, one can only modify the relevant microgrid section in the model. The

proposed models are also suitable for digital twin applications and real-time simulations due to their high precision and low computational requirements.

CRediT authorship contribution statement

Declaration of competing interest

The authors declare that they have no known competing financial interests or personal relationships that could have appeared to influence the work reported in this paper.

Data availability

The authors do not have permission to share data.

Acknowledgements

Appendix A. . Sensitivity analysis results of C-BESS

The sensitivity analysis results of a C-BESS in a DC microgrid are shown in Fig. A1. Additionally, the eigenvalue loci of the RC-pairs are the same as those of a V-BESS in a DC microgrid, and the eigenvalue locus of P3 is omitted here due to its insignificant effect.
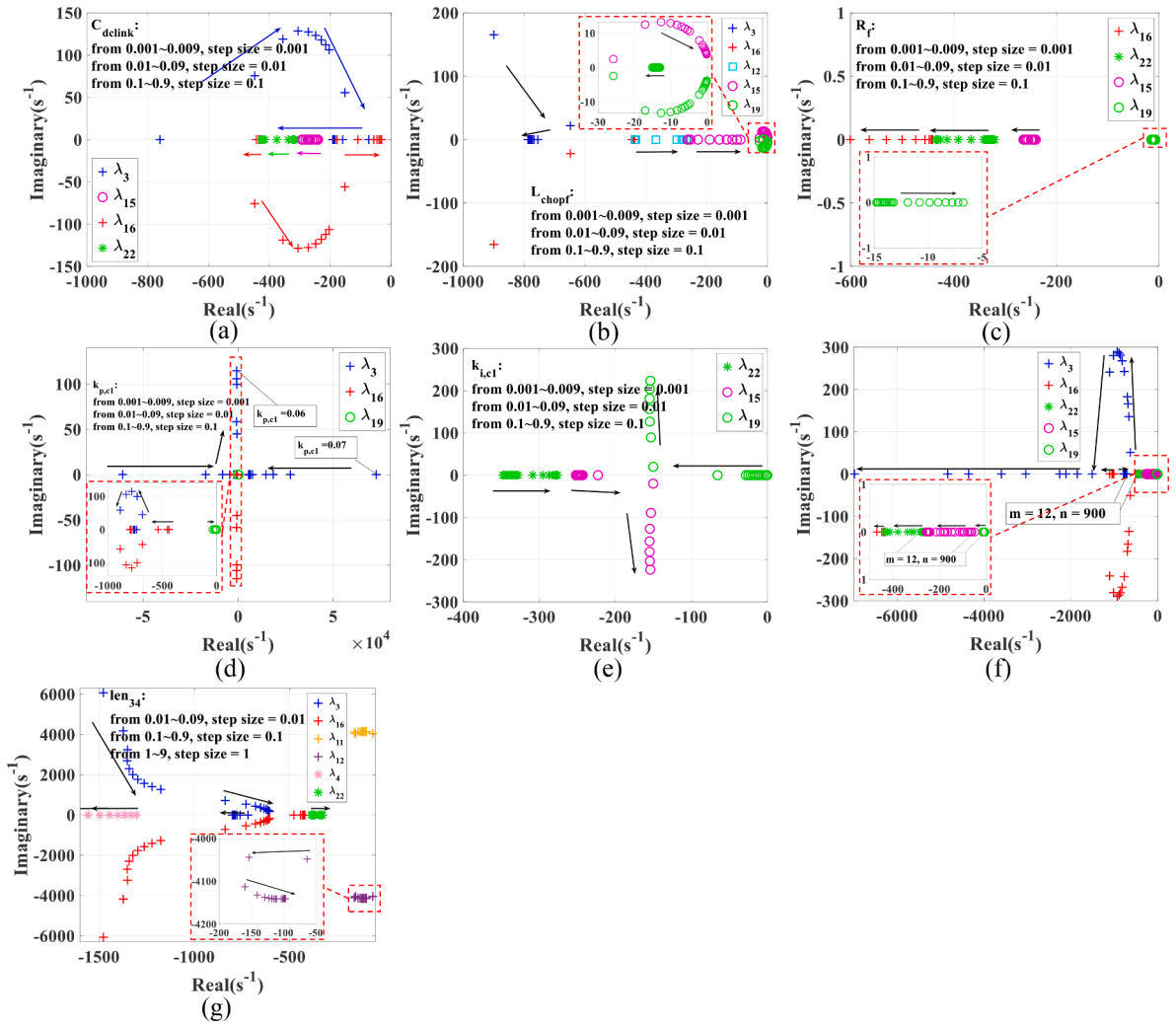

Fig. A1. Eigenvalue loci of system parameter variations (C-BESS): (a) DC bus capacitance C_{dclink}, (b) Filter inductance L_f, (c) Filter resistance R_f, (d) Controller parameter $k_{p, c1}$, (e) Controller parameter $k_{i, c1}$, (f) Cells connection number m and n, (g) Delivery line 34 length len_{34}.

References

[1] Tan KM, Babu TS, Ramachandaramurthy VK, Kasinathan P, Solanki SG, Raveendran SK. Empowering smart grid: a comprehensive review of energy storage technology and application with renewable energy integration. J Energy Storage 2021;39:102591. https://doi.org/10.1016/j.est.2021.102591.

[2] Liu J, Hu C, Kimber A, Wang Z. Uses, cost-benefit analysis, and markets of energy storage systems for electric grid applications. J Energy Storage 2020;32:101731. https://doi.org/10.1016/j.est.2020.101731.

[3] Killer M, Farrokhseresht M, Paterakis NG. Implementation of large-scale Li-ion battery energy storage systems within the EMEA region. Appl Energy 2020;260: 114166. https://doi.org/10.1016/j.apenergy.2019.114166.

[4] Wei X, Amin MA, Xu Y, Jing T, Yi Z, Wang X, et al. Two-stage cooperative intelligent home energy management system for optimal scheduling. IEEE Trans Ind Appl 2022;58:5423–37. https://doi.org/10.1109/TIA.2022.3172669.

[5] Hafsi O, Abdelkhalek O, Mekhilef S, Soumeur MA, Hartani MA, Chakar A. Integration of hydrogen technology and energy management comparison for DC-Microgrid including renewable energies and energy storage system. Sustain Energy Technol Assess 2022;52:102121. https://doi.org/10.1016/j.seta.2022.102121.

[6] Bhosale R, Agarwal V. Fuzzy logic control of the ultracapacitor interface for enhanced transient response and voltage stability of a DC microgrid. IEEE Trans Ind Appl 2019;55:712–20. https://doi.org/10.1109/TIA.2018.2870349.

[7] Hosseini SA, Toulabi M, Ashouri-Zadeh A, Ranjbar AM. Battery energy storage systems and demand response applied to power system frequency control. Int J Electr Power Energy Syst 2022;136:107680. https://doi.org/10.1016/j.ijepes.2021.107680.

[8] Bazargan D, Filizadeh S, Gole AM. Stability analysis of converter-connected battery energy storage systems in the grid. IEEE Trans Sustain Energy 2014;5:1204–12. https://doi.org/10.1109/TSTE.2014.2337053.

[9] Saad AA, Faddel S, Youssef T, Mohammed O. Small-signal model predictive control based resilient energy storage management strategy for all electric ship MVDC voltage stabilization. J Energy Storage 2019;21:370–82. https://doi.org/10.1016/j.est.2018.12.009.

[10] Liang Y, Pan C, Zhang J. Current trajectory coefficient based time domain line protection for battery storage energy stations. J Energy Storage 2022;51:104468. https://doi.org/10.1016/j.est.2022.104468.

[11] Ghenai C, Husein LA, Al Nahlawi M, Hamid AK, Bettayeb M. Recent trends of digital twin technologies in the energy sector: a comprehensive review. Sustain Energy Technol Assess 2022;54:102837. https://doi.org/10.1016/j.seta.2022.102837.

[12] Lu C-F. Dynamic modelling of battery energy storage system and application to power system stability. IEE Proc - Gener Transm Distrib 1995;142:429. https://doi.org/10.1049/ip-gtd:19951858.

[13] Ortega Á, Milano F. Generalized model of VSC-based energy storage systems for transient stability analysis. IEEE Trans Power Syst 2016;31:3369–80. https://doi.org/10.1109/TPWRS.2015.2496217.

[14] Farrokhabadi M, König S, Cañizares CA, Bhattacharya K, Leibfried T. Battery energy storage system models for microgrid stability analysis and dynamic simulation. IEEE Trans Power Syst 2018;33:2301–12. https://doi.org/10.1109/TPWRS.2017.2740163.

[15] Dubarry M, Baure G, Pastor-Fernández C, Yu TF, Widanage WD, Marco J. Battery energy storage system modeling: a combined comprehensive approach. J Energy Storage 2019;21:172–85. https://doi.org/10.1016/j.est.2018.11.012.

[16] Calero F, Cañizares CA, Bhattacharya K. Dynamic modeling of battery energy storage and applications in transmission systems. IEEE Trans Smart Grid 2021;12: 589–98. https://doi.org/10.1109/TSG.2020.3016298.

[17] Berger M, Kocar I, Farantatos E, Haddadi A. Modeling of Li-ion battery energy storage systems (BESSs) for grid fault analysis. Electr Pow Syst Res 2021;196: 107160. https://doi.org/10.1016/j.epsr.2021.107160.

[18] Xing W, Wang H, Lu L, Han X, Sun K, Ouyang M. An adaptive virtual inertia control strategy for distributed battery energy storage system in microgrids. Energy 2021; 233:121155. https://doi.org/10.1016/j.energy.2021.121155.

[19] Weber LG, Nasiri A, Akbari H. Dynamic modeling and control of a synchronous generator in an AC microgrid environment. IEEE Trans Ind Appl 2018;54:4833–41. https://doi.org/10.1109/TIA.2018.2845392.

[20] Kim M, Lee SG, Bae S. Decentralized power management for electrical power systems in more electric aircrafts. Electronics 2018;7:187. https://doi.org/10.3390/electronics7090187.

[21] Rajasekaran S, Suresh S, Ramkumar A, Karthikeyan K. A novel solar photovoltaic integrated modified SEPIC high gain DC–DC converter using evolutionary algorithms for electric vehicle battery applications. J Electr Eng Technol 2023;18: 3681–94. https://doi.org/10.1007/s42835-023-01459-2.

[22] Baidya S, Nandi C. A comprehensive review on DC Microgrid protection schemes. Electr Pow Syst Res 2022;210:108051. https://doi.org/10.1016/j.epsr.2022.108051.

[23] Dragičević T, Lu X, Vasquez JC, Guerrero JM. DC microgrids—Part I: a review of control strategies and stabilization techniques. IEEE Trans Power Electron 2016; 31:4876–91. https://doi.org/10.1109/TPEL.2015.2478859.

[24] Kumar J, Agarwal A, Agarwal V. A review on overall control of DC microgrids. J Energy Storage 2019;21:113–38. https://doi.org/10.1016/j.est.2018.11.013.

[25] Leng M, Zhou G, Xu G, Sahoo S, Liu X, Zhou Q, et al. Small-signal stability assessment and interaction analysis for bipolar DC microgrids. IEEE Trans Power Electron 2023;38:5524–37. https://doi.org/10.1109/TPEL.2022.3233397.

[26] Sahoo H, Kapat S, Singh B. Small-Signal modeling and analysis of converter interactivity in 48 V DC grid. IEEE Trans Ind Appl 2023;59:5622–32. https://doi.org/10.1109/TIA.2023.3275884.

[27] Derbas AA, Oshnoei A, Azzouz MA, Awad ASA, Blaabjerg F, Anvari-Moghaddam A. Adaptive damping control to enhance small-signal stability of DC microgrids. IEEE J Emerg Sel Top Power Electron 2023;11:2963–78. https://doi.org/10.1109/JESTPE.2023.3236809.

[28] Lawder MT, Suthar B, Northrop PWC, De S, Hoff CM, Leitermann O, et al. Battery energy storage system (BESS) and battery management system (BMS) for grid-scale applications. Proc IEEE 2014;102:1014–30. https://doi.org/10.1109/JPROC.2014.2317451.

[29] Zhang W, Wang D, Zheng W. A semiconductor-electrochemistry model for design of high-rate Li ion battery. J Energy Chem 2020;41:100–6. https://doi.org/10.1016/j.jechem.2019.04.018.

[30] Chen M, Rincon-Mora GA. Accurate electrical battery model capable of predicting runtime and I-V performance. IEEE Trans Energy Convers 2006;21:504–11. https://doi.org/10.1109/TEC.2006.874229.

[31] Johnson VH. Battery performance models in ADVISOR. J Power Sources 2002;110: 321–9. https://doi.org/10.1016/S0378-7753(02)00194-5.

[32] He W, Williard N, Chen C, Pecht M. State of charge estimation for Li-ion batteries using neural network modeling and unscented Kalman filter-based error cancellation. Int J Electr Power Energy Syst 2014;62:783–91. https://doi.org/10.1016/j.ijepes.2014.04.059.

[33] Xing Y, He W, Pecht M, Tsui KL. State of charge estimation of lithium-ion batteries using the open-circuit voltage at various ambient temperatures. Appl Energy 2014; 113:106–15. https://doi.org/10.1016/j.apenergy.2013.07.008.

[34] Jeong D, Bae S. Estimating battery state-of-charge with a few target training data by meta-learning. J Power Sources 2023;553:232238. https://doi.org/10.1016/j.jpowsour.2022.232238.

[35] Huang C-S. A lithium-ion batteries fault diagnosis method for accurate coulomb counting state-of-charge estimation. J Electr Eng Technol 2024;19:433–42. https://doi.org/10.1007/s42835-023-01533-9.

[36] Chung D-W, Ko J-H, Yoon K-Y. State-of-charge estimation of lithium-ion batteries using LSTM deep learning method. J Electr Eng Technol 2022;17:1931–45. https://doi.org/10.1007/s42835-021-00954-8.

[37] Alam MS, Al-Ismail FS, Al-Sulaiman FA, MohammadA A. Energy management in DC microgrid with an efficient voltage compensation mechanism. Electr Pow Syst Res 2023;214:108842. https://doi.org/10.1016/j.epsr.2022.108842.

[38] Ferahtia S, Djerioui A, Rezk H, Chouder A, Houari A, Machmoum M. Adaptive droop based control strategy for DC microgrid including multiple batteries energy storage systems. J Energy Storage 2022;48:103983. https://doi.org/10.1016/j.est.2022.103983.

[39] Adly M, Strunz K. DC microgrid small-signal stability and control: Sufficient stability criterion and stabilizer design. Sustain Energy Grids Netw 2021;26: 100435. https://doi.org/10.1016/j.segan.2021.100435.

[40] Kundur P. Power System Stability and Control. McGraw-Hill; 1994.

[41] Linear Analysis and Small-Signal Stability. Power Syst. Model. Comput. Control, John Wiley & Sons, Ltd; 2019, p. 149–73. doi: 10.1002/9781119546924.ch6.

[42] Anand S, Fernandes BG. Reduced-order model and stability analysis of low-voltage DC microgrid. IEEE Trans Ind Electron 2013;60:5040–9. https://doi.org/10.1109/TIE.2012.2227902.